

Modeling Porous Dust Grains with Ballistic Aggregates I: Geometry and Optical Properties

Yue Shen, B. T. Draine, and Eric T. Johnson

Princeton University Observatory, Princeton, NJ 08544, USA

ABSTRACT

We investigate the scattering and absorption of light by random ballistic aggregates of spherical monomers. We present general measures for the size, shape, and porosity of an irregular particle. Three different classes of ballistic aggregates are considered, with different degrees of porosity. Scattering and absorption cross sections are calculated, using the discrete dipole approximation (DDA), for grains of three compositions (50% silicate and 50% graphite; 50% silicate and 50% amorphous carbon; and 100% silicate, where percentages are by volume), for wavelengths from $0.1 \mu\text{m}$ to $4 \mu\text{m}$. For fixed amount of solid material, increased porosity increases the extinction at short wavelengths, but decreases the extinction at wavelengths long compared to the overall aggregate size. Scattering and absorption cross sections are insensitive to monomer size as long as the constituent monomers are small compared with the incident wavelength. We compare our accurate DDA results with two other approximations: the analytical multi-layer sphere (MLS) model and effective medium theory (EMT). For high porosity and/or absorptive materials, the MLS model does not provide a good approximation for scattering and absorption by ballistic aggregates. The EMT method provides a much better approximation than the MLS model for these aggregates, with a typical difference $\lesssim 20\%$ in extinction and scattering cross sections compared with DDA results, for all types, compositions and wavelengths probed in this study.

Subject headings: dust, extinction – scattering – circumstellar matter – interplanetary medium

1. Introduction

The appearance of star-forming galaxies is strongly affected by interstellar dust. Starlight is absorbed and scattered by dust particles, and the absorbed energy is predominantly reradiated at infrared wavelengths. The optical properties of the dust must be characterized in order to determine the spectra and spatial distribution of the stars (i.e., to “correct” for reddening and extinction), and to interpret the observed infrared emission. Characterizing the dust is also important for more fundamental reasons: dust grains play an important role in the thermodynamics and chemistry of the interstellar medium (e.g., heating from photoelectric emission, and grain catalysis of H_2), in

interstellar gas dynamics (e.g., radiation pressure on dust grains), and in the formation of stars, planets, and planetesimals.

Many interplanetary dust particles (IDPs) are irregular, fluffy aggregates, sometimes described as having a “fractal” appearance. Direct evidence comes from such IDPs collected by high-flying aircraft (Brownlee 1985; Warren et al. 1994). Laboratory and microgravity experiments of dust particle interactions, which may mimic the conditions in the early solar system, also suggest that particles form fractal assemblies through ballistic aggregation (Wurm & Blum 1998; Blum & Wurm 2000; Krause & Blum 2004). Similar aggregation processes may well occur in interstellar environments, where small dust grains coagulate in dense molecular clouds (Dorschner & Henning 1995). A number of authors have proposed that interstellar grains consist primarily of such aggregate structures, with a random, porous geometry (e.g., Mathis & Whiffen 1989).

Aggregates are irregular, porous, particle assemblies, possibly incorporating multiple materials. Early attempts to estimate the optical properties of such structures used a combination of Mie theory and effective medium theory (EMT), where an aggregate is approximated by a homogeneous sphere with an “effective” refractive index intended to allow for the effects of porosity (e.g., Mathis 1996; Li & Greenberg 1998). Alternatively, Voshchinnikov & Mathis (1999) proposed a multi-layer sphere (MLS) model to account for porous, composite dust grains. The advantage of this MLS model is that, just as for homogeneous spheres, the solution is exact and can be obtained via a fast algorithm (Wu et al. 1997). The limitations are: the grains are assumed to be spherical, and all compositions (including vacuum) are assumed to be well mixed inside the sphere. Comparisons of the MLS with EMT-Mie theory are done by Voshchinnikov et al. (2005, 2006), suggesting that the MLS model is accurate for spherical, well-mixed dust grains, for certain compositions and porosities. So far there has been no study of whether or not the MLS prescription is also suitable for irregular aggregates.

Solving Maxwell’s equations becomes increasingly challenging when the geometry departs from spheres. Several methods have been developed to compute light scattering by non-spherical particles. The “extended boundary condition method” (EBCM) introduced by Waterman (1971), and developed by Mishchenko & Travis (1994) and Wielaard et al. (1997) can be applied to solid targets with relatively smooth surfaces, and exact series expansions have been developed for spheroids (Asano & Yamamoto 1975; Asano & Sato 1980; Voshchinnikov & Farafonov 1993; Farafonov et al. 1996), but these techniques cannot be applied to the complex geometries of interest here. The special case of clusters of spheres can also be treated by superposition of vector spherical harmonics (Mackowski 1991; Xu 1997), sometimes referred to as the generalized multisphere Mie (GMM) solution. If the complete T-matrix can be found for the individual particles, the T-matrix for a cluster can, in principle, be found using the superposition T-matrix method (TMM, e.g., Mackowski & Mishchenko 1996). However, these techniques, although formally exact, can prove very computationally-demanding when applied to spheres that are numerous and in close proximity (e.g., in contact), particularly when the refractive index differs appreciably from vacuum.

The discrete dipole approximation (DDA) method (e.g., Purcell & Pennypacker 1973; Draine & Flatau 1994) is the most flexible among all the methods, although substantial computational resources may be needed in order to achieve the desired accuracy. Using either GMM, TMM or DDA, the optical properties of different kinds of aggregates have been investigated extensively during the past decade (e.g., West 1991; Lumme & Rahola 1994; Petrova et al. 2000; Kimura et al. 2006; Bertini et al. 2007); most of these investigations are applied to cometary dust.

There is increasing interest in the possibility that interstellar and circumstellar grains may be porous, random aggregates. To confront this hypothesis with observational data, it is necessary to calculate the optical properties of such aggregates. The calculations must be carried out for a wide range of wavelengths - from infrared to vacuum ultraviolet - and for aggregates with potentially realistic geometry and composition. Massive computations are required to attain these goals.

In this paper, we use the DDA to calculate scattering and absorption for a large sample of aggregates with different compositions, sizes, and porosities, over a wide range of wavelength. We explore the dependence of various optical properties on wavelength, grain size, aggregate geometry, as well as compositions, and we investigate the applicability of multi-layer sphere calculations and the EMT-Mie model to these random aggregates.

Characterization of the size, gross shape, and porosity of an irregular particle is discussed in §2. §3 describes procedures for generating random aggregates (“BAM1” and “BAM2”) that are less porous than the standard ballistic aggregates, and §4 discusses the applicability of the DDA method to these aggregates.

Extinction and absorption behaviors are presented in §5, with comparison to the MLS model in §5.3, and comparison to the EMT-Mie model in §5.4. Our results are summarized and discussed in §6. Applications to circumstellar debris disks and cometary dust will be presented in a companion paper (Shen et al. 2007, hereafter Paper II).

2. Geometric Properties of Irregular Particles

In general, we define the “effective radius” (or “volume equivalent radius”) of a general 3-dimensional structure to be the radius of a sphere with volume equal to the volume V of solid material in the structure:

$$a_{\text{eff}} \equiv \left(\frac{3V}{4\pi} \right)^{1/3}. \quad (1)$$

There are several possible ways to quantify the “porosity” or openness of the structure, depending on how to measure its apparent size. Different definitions of the apparent size for a fluffy structure have been used, i.e., based on the radius of gyration (e.g., Kozasa et al. 1992) or using the geometric cross section (e.g., Ossenkopf 1993).

Here we propose a simple but general way to quantify the size, shape and porosity of a finite

structure with arbitrary geometry. Let the “density” $\rho_0 = 1$ at points within solid material, and $\rho_0 = 0$ otherwise.¹ Let \mathbf{I} be the moment of inertia tensor of the structure, with eigenvalues $I_1 \geq I_2 \geq I_3$. It is convenient to define dimensionless quantities

$$\alpha_i \equiv \frac{I_i}{0.4Ma_{\text{eff}}^2} \quad (2)$$

where $M \equiv \rho_0 V$. For a target that is a solid sphere, $\alpha_i = 1$.

We characterize the size and shape of an irregular structure by considering an “equivalent ellipsoid” of uniform density $f\rho_0$ and semi-major axes $a \leq b \leq c$. The quantities (f, a, b, c) are uniquely determined by requiring that the mass M and principal components of the moment of inertia I_i of the target and its equivalent ellipsoid be identical, such that:

$$\frac{4\pi}{3}\rho_0 a_{\text{eff}}^3 = f\rho_0 \frac{4\pi}{3}abc \quad (3)$$

$$\frac{8\pi}{15}\rho_0 a_{\text{eff}}^5 \alpha_1 = f\rho_0 \frac{4\pi}{15}abc(b^2 + c^2) \quad (4)$$

$$\frac{8\pi}{15}\rho_0 a_{\text{eff}}^5 \alpha_2 = f\rho_0 \frac{4\pi}{15}abc(a^2 + c^2) \quad (5)$$

$$\frac{8\pi}{15}\rho_0 a_{\text{eff}}^5 \alpha_3 = f\rho_0 \frac{4\pi}{15}abc(a^2 + b^2) \quad (6)$$

with solutions

$$a = (\alpha_2 + \alpha_3 - \alpha_1)^{1/2} a_{\text{eff}} \quad (7)$$

$$b = (\alpha_3 + \alpha_1 - \alpha_2)^{1/2} a_{\text{eff}} \quad (8)$$

$$c = (\alpha_1 + \alpha_2 - \alpha_3)^{1/2} a_{\text{eff}} \quad (9)$$

$$f = [(\alpha_2 + \alpha_3 - \alpha_1)(\alpha_3 + \alpha_1 - \alpha_2)(\alpha_1 + \alpha_2 - \alpha_3)]^{-1/2} \quad (10)$$

f from eq. (10) is then the volume filling factor for the equivalent ellipsoid. We define a characteristic size

$$R_{abc} \equiv (abc)^{1/3} = [(\alpha_2 + \alpha_3 - \alpha_1)(\alpha_3 + \alpha_1 - \alpha_2)(\alpha_1 + \alpha_2 - \alpha_3)]^{1/6} a_{\text{eff}} \quad (11)$$

which is simply the radius of a sphere with a volume equal to the equivalent ellipsoid defined above; the filling factor is just $f = (a_{\text{eff}}/R_{abc})^3$. We define the “porosity” to be

$$\mathcal{P} \equiv 1 - f = 1 - (a_{\text{eff}}/R_{abc})^3 \quad (12)$$

Kozasa et al. (1992) characterized the overall size of the structure by a radius proportional to the radius of gyration:

$$R_{\text{KBM}} \equiv \left[\frac{\alpha_1 + \alpha_2 + \alpha_3}{3} \right]^{1/2} a_{\text{eff}} \quad (13)$$

¹We are discussing purely geometric properties of the target, which are independent of the actual material density. The function ρ_0 is here introduced to allow use of familiar concepts like total mass and moment-of-inertia tensor, but should be understood to indicate “occupation” if $\rho_0 = 1$, and vacuum if $\rho_0 = 0$.

For a uniform density target, $R_{\text{KBM}} = (5/3)^{1/2} R_{\text{gyr}}$, where R_{gyr} is the radius of gyration. Kozasa et al. (1992) proposed that the porosity be based on the ratio between R_{KBM} and a_{eff} :

$$P_{\text{KBM}} \equiv 1 - (a_{\text{eff}}/R_{\text{KBM}})^3 \quad (14)$$

Finally, one can also define a radius

$$R_{\text{proj}} \equiv [\langle C_{\text{proj}} \rangle / \pi]^{1/2} \quad , \quad (15)$$

where $\langle C_{\text{proj}} \rangle$ is the orientation-averaged projected area of the target. For irregular targets, R_{proj} is more difficult to compute than either R_{abc} or R_{KBM} . These three radii – R_{abc} , R_{KBM} , and R_{proj} – will be compared below for the ballistic aggregates in this study.

The gross shape of the target can be characterized by the ratios c/b and b/a , where a, b, c are given by eq. (7-9). We will refer to agglomerates as oblate if $c/b < b/a$, and prolate if $c/b > b/a$.

It is convenient to define dimensionless efficiency factors Q for absorption, scattering and extinction:

$$Q(\lambda) \equiv \frac{C(\lambda)}{\pi a_{\text{eff}}^2} \quad , \quad (16)$$

where $C(\lambda)$ is the cross-section for absorption, scattering, or extinction, and a_{eff} is the solid-volume-equivalent radius, defined by eq. (1).

3. Geometric Properties of Ballistic Aggregates

We use 3 simple algorithms for generating irregular porous structures with varying degrees of porosity. The first is standard “ballistic agglomeration” (BA), sometimes referred to as “ballistic particle-cluster agglomeration” (BPCA), previously discussed by many authors (e.g., West 1991; Kozasa et al. 1992, 1993; Ossenkopf 1993; Kimura et al. 2006; Bertini et al. 2007). We also introduce two new prescriptions for agglomeration – BAM1 and BAM2 – that produce random structures that are less “fluffy” than those produced by BA (see §3.1).

Random aggregates can be characterized by the Hausdorff dimension D (sometimes referred to as the fractal dimensionality), with mass $M \propto R^D$ as $R \rightarrow \infty$ where R is some characteristic size of the agglomerate. The filling factor $f \propto M/R^3 \propto M^{1-3/D}$. All three agglomeration algorithms employed here (BA, BAM1, BAM2) are thought to have Hausdorff dimension $D \approx 3$, with the filling factor $f \rightarrow \text{constant}$ as $M \rightarrow \infty$.

Other processes have also been proposed for generating random agglomerates, including ballistic cluster-cluster aggregation” (BCCA) and diffusion-limited aggregation (DLA). BCCA clusters obtained by random aggregation of clusters with equal-mass clusters are very “fluffy”, with $D \approx 2.25$ (Kozasa et al. 1993) and filling factor $f \propto M^{-0.33}$. Clusters produced by diffusion-limited aggregation have a dendritic appearance, with $D \approx 2.5$ (Witten & Cates 1986), and $f \propto M^{-0.2}$. We

do not consider either BCCA clusters or DLA clusters here, because their fragile geometries seem unlikely to be representative of circumstellar or interstellar grains, which are subject to occasional grain-grain collisions.

We stress that we do not claim that any of our algorithms (BA, BAM1, or BAM2) provides a realistic representation of the actual processes responsible for the growth of circumstellar or interstellar grains – they are merely convenient procedures for generating irregular targets that may bear some geometric resemblance to real circumstellar or interstellar grains.

3.1. Target Generation

We construct clusters (“targets”) by random ballistic agglomeration. Each cluster is composed of a certain number of spheres (or “monomers”) of a single radius a_0 . The agglomeration process begins with one monomer ($j = 1$). A cluster is built up by sequential arrival of additional monomers ($j = 2, \dots, N$) on random rectilinear trajectories. We consider three different classes of clusters, distinguished by aggregation rules.

BA (“ballistic agglomeration”) clusters are produced by requiring arriving monomers to “stick” at the point where they first contact the preexisting aggregate. This is a well-established procedure (e.g., West 1991; Kozasa et al. 1992, 1993; Ossenkopf 1993; Kimura et al. 2006; Bertini et al. 2007), also known as “Ballistic Particle-Cluster Aggregation” (BPCA). Clusters formed in this way have fractal dimension ≈ 3 , but high porosity. Figure 1 (top row) shows examples of BA clusters with $N = 256, 1024, 4096$ monomers.

BAM1 (“ballistic agglomeration with one migration”) clusters are produced by requiring arriving monomers $j \geq 3$, after making first contact with a monomer $k < j$, to “migrate” to make contact with another monomer, by rolling or sliding over the first-contacted monomer, along the shortest possible trajectory. If there is more than one candidate for this second contact, the nearer is chosen. BAM1 clusters with $N \geq 3$ have every monomer in contact with at least two other monomers; for $N \geq 4$ some of the monomers are in contact with three or more other monomers. Figure 1 (middle row) shows BAM1 clusters with $N = 256, 1024, 4096$ monomers.

BAM2 clusters are constructed as follows: monomers $j = 2$ and 3 are added randomly just as for the BAM1 clusters. Monomers $j \geq 4$ arrive on random rectilinear trajectories; after first contact they make *two* migrations. The first migration is the same as for constructing BAM1 clusters: “rolling” along the shortest possible trajectory to make a second contact. This is followed by a second migration, now rolling over both the first and second sphere contacted to contact a third neighbor, again choosing the shortest trajectory if there is more than one candidate. BAM2 clusters with $N \geq 4$ have every monomer in contact with at least three neighbors, with some in contact with four or more neighbors. Figure 1 (bottom row) shows examples of BAM2 clusters with $N = 256, 1024, 4096$ monomers.

For clusters consisting of N spherical monomers of radius a_0 we have,

$$a_{\text{eff}} = N^{1/3}a_0 . \quad (17)$$

We generated clusters using the BA, BAM1, and BAM2 algorithms, for a large number of different seeds for the random number generator. A library of samples is available² for $N = 2^3, 2^4, \dots, 2^{16}$. Below we report the statistical properties of such clusters.

3.2. Size and Porosity of Ballistic Aggregates

The clusters formed following the above procedure are generally irregular and “porous”, with the porosity decreasing from BA to BAM1 to BAM2, as is apparent from comparison of the three rows in Fig. 1.

For a given N and aggregation rule, the characteristic size R_{abc} will vary from realization to realization because the aggregation process is random. Figure 2 shows the expectation value $\langle R_{abc} \rangle$ based on many random realizations, for $N = 2^3, 2^4, \dots, 2^{16}$; the realization-to-realization variations are also shown. The BA clusters have $\langle R_{abc} \rangle \rightarrow 2.0a_{\text{eff}}$ as $N \rightarrow \infty$, the BAM1 clusters have $\langle R_{abc} \rangle \rightarrow 1.7a_{\text{eff}}$, and the BAM2 clusters have $\langle R_{abc} \rangle \rightarrow 1.5a_{\text{eff}}$. Note, however, that even for $N > 10^4$, the $\langle R_{abc}/a_{\text{eff}} \rangle$ continues to increase as N increases from 2^{14} to 2^{15} to 2^{16} , so the limiting values for $N \rightarrow \infty$ are uncertain. Figure 2 also shows $\langle R_{\text{KBM}} \rangle$, the characteristic size given by eq. (13). For $N > 10^4$, $R_{\text{KBM}} \approx R_{abc}$. However, for smaller N R_{KBM} is noticeably larger than R_{abc} . In addition, the realization-to-realization variation in R_{KBM} is appreciably larger than for R_{abc} . We consider R_{abc} to be the better way to characterize the effective size of a random structure.

For each of our clusters, we have estimated the orientation-averaged projected area, and from this the radius R_{proj} . These computations are time-consuming; the computation is carried out by enclosing the target within a sphere of radius R_c , choosing N_r points at random on the sphere, for each such point choosing a random inward direction (drawn from a distribution corresponding to isotropic incidence on the sphere), and determining whether that ray does or does not intersect the target structure. If the number of intersecting rays is N_x , then $R_{\text{proj}} = \sqrt{N_x/N_r}R_c$. We typically employ $N_r = 10^6$ in order to achieve accuracy better than 1% in the determination of R_{proj} . It is striking that, for a given N , R_{proj} in Figure 2 shows less realization-to-realization variation than even R_{abc} .

The expectation values $\langle f \rangle$ and $\langle \mathcal{P} \rangle = 1 - \langle f \rangle$ are shown in Figure 3. For large N , the BA clusters have $\langle \mathcal{P} \rangle \approx 0.87$, whereas the BAM2 clusters have substantially lower porosity, $\langle \mathcal{P} \rangle \approx 0.70$.

Validation of a code to generate random clusters is not simple, but can be done by comparing the statistical properties of the clusters with those of other Monte Carlo cluster generators. Statis-

² [http://www.astro.princeton.edu/~sim\\$draine/agglom.html](http://www.astro.princeton.edu/~sim$draine/agglom.html)

Table 1. Sizes of BA, BAM1, and BAM2 Clusters

N	Characteristic Radius R_{abc}/a_{eff} ^a from eq. (11)			Radius R_{KBM} ^a from eq. (13)			Projected Area Radius R_{proj} ^b		
	BA	BAM1	BAM2	BA	BAM1	BAM2	BA	BAM1	BAM2
8	1.4300 ± 0.0732	1.2435 ± 0.0287	1.1569 ± 0.0136	1.7049 ± 0.1683	1.3786 ± 0.0650	1.2133 ± 0.0230	1.2569 ± 0.0163	1.1979 ± 0.0116	1.1458 ± 0.0057
16	1.5885 ± 0.0868	1.3304 ± 0.0367	1.1860 ± 0.0167	1.8209 ± 0.1671	1.4611 ± 0.0828	1.2526 ± 0.0453	1.3514 ± 0.0197	1.2670 ± 0.0158	1.1861 ± 0.0106
32	1.7060 ± 0.0884	1.4079 ± 0.0440	1.2212 ± 0.0228	1.8906 ± 0.1486	1.5242 ± 0.0838	1.2910 ± 0.0521	1.4469 ± 0.0219	1.3362 ± 0.0183	1.2288 ± 0.0138
64	1.7861 ± 0.0794	1.4733 ± 0.0454	1.2614 ± 0.0271	1.9262 ± 0.1227	1.5684 ± 0.0751	1.3258 ± 0.0501	1.5405 ± 0.0227	1.4036 ± 0.0194	1.2727 ± 0.0155
128	1.8371 ± 0.0668	1.5262 ± 0.0427	1.2998 ± 0.0284	1.9403 ± 0.0966	1.5991 ± 0.0628	1.3530 ± 0.0450	1.6299 ± 0.0225	1.4681 ± 0.0193	1.3146 ± 0.0165
256	1.8705 ± 0.0535	1.5650 ± 0.0356	1.3340 ± 0.0271	1.9464 ± 0.0745	1.6190 ± 0.0498	1.3759 ± 0.0381	1.7138 ± 0.0216	1.5277 ± 0.0182	1.3552 ± 0.0165
512	1.8914 ± 0.0418	1.5932 ± 0.0296	1.3633 ± 0.0245	1.9470 ± 0.0565	1.6325 ± 0.0396	1.3949 ± 0.0323	1.7894 ± 0.0199	1.5814 ± 0.0171	1.3940 ± 0.0161
1024	1.9052 ± 0.0329	1.6157 ± 0.0243	1.3899 ± 0.0202	1.9454 ± 0.0429	1.6428 ± 0.0297	1.4130 ± 0.0254	1.8556 ± 0.0183	1.6289 ± 0.0158	1.4315 ± 0.0144
2048	1.9177 ± 0.0248	1.6343 ± 0.0183	1.4114 ± 0.0171	1.9467 ± 0.0322	1.6535 ± 0.0225	1.4274 ± 0.0207	1.9131 ± 0.0160	1.6708 ± 0.0141	1.4647 ± 0.0130
4096	1.9286 ± 0.0198	1.6500 ± 0.0151	1.4300 ± 0.0135	1.9493 ± 0.0250	1.6630 ± 0.0175	1.4409 ± 0.0159	1.9612 ± 0.0148	1.7060 ± 0.0126	1.4934 ± 0.0110
8192	1.9384 ± 0.0151	1.6631 ± 0.0115	1.4462 ± 0.0114	1.9532 ± 0.0174	1.6718 ± 0.0130	1.4533 ± 0.0122	2.0002 ± 0.0130	1.7344 ± 0.0101	1.5177 ± 0.0095
16384	1.9508 ± 0.0121	1.6758 ± 0.0097	1.4588 ± 0.0082	1.9606 ± 0.0129	1.6828 ± 0.0113	1.4640 ± 0.0088	2.0334 ± 0.0110	1.7574 ± 0.0093	1.5363 ± 0.0068
32768	1.9620 ± 0.0089	1.6875 ± 0.0073	1.4714 ± 0.0063	1.9691 ± 0.0091	1.6926 ± 0.0089	1.4751 ± 0.0066	2.0586 ± 0.0079	1.7762 ± 0.0073	1.5531 ± 0.0065
65536	1.9771 ± 0.0076	1.6996 ± 0.0056	1.4835 ± 0.0036	1.9811 ± 0.0089	1.7032 ± 0.0067	1.4862 ± 0.0040	2.0795 ± 0.0086	1.7924 ± 0.0063	1.5664 ± 0.0041

^a Mean and $\pm 1\sigma$ realization-to-realization variation in R_{abc} from eq. (11).

^a Mean and $\pm 1\sigma$ realization-to-realization variation in R_{KBM} from eq. (13).

^b Mean and $\pm 1\sigma$ realization-to-realization variation in R_{proj} from eq. (15).

tical properties of the three types of aggregate clusters are given in Tables 1 and 2 for cluster sizes ranging from $N = 2^3$ to $N = 2^{16}$.

The BA clusters have been frequently used in the literature (e.g., Kozasa et al. 1992, 1993; Ossenkopf 1993; Kimura et al. 2006; Bertini et al. 2007). For the same N , our calculated projected areas agree with results for BA clusters reported by Kozasa et al. (1993) and Nakamura et al. (1994) as shown in Figure 2 (top panel). However, as seen in Figure 2 (middle panel), our values of R_{KBM} (defined by eq. 13) are slightly lower than the results reported by Kozasa et al. (1993). The reason for this discrepancy is not known.³

3.3. Shape of Ballistic Aggregates

The axial ratios c/b and b/a give an indication of the overall shape of each random aggregate. Figure 4 shows c/b and b/a for BA, BAM1, and BAM2 clusters with $N = 2^6, 2^8, 2^{10},$ and 2^{12} spheres. For a given N , the sequence BA \rightarrow BAM1 \rightarrow BAM2 corresponds to decreasing eccentricity. Similarly, for a given agglomeration rule (BA, BAM1, or BAM2), clusters with larger N tend to be more spherical.

³ T. Kozasa has kindly provided several BA clusters from Kozasa et al. (1993). For these clusters, we obtain values of R_{abc}/a_{eff} and $R_{\text{KBM}}/a_{\text{eff}}$ that are consistent with the statistics reported in our Table 1.

Table 2. Porosities of BA, BAM1, and BAM2 Clusters

N	Porosity \mathcal{P}^a from eq. (12)			Porosity P_{KBM}^b		
	BA	BAM1	BAM2	BA	BAM1	BAM2
8	0.6580 \pm 0.0525	0.4799 \pm 0.0360	0.3541 \pm 0.0228	0.7982 \pm 0.0598	0.6183 \pm 0.0540	0.4402 \pm 0.0319
16	0.7505 \pm 0.0409	0.5753 \pm 0.0351	0.4006 \pm 0.0253	0.8265 \pm 0.0443	0.6736 \pm 0.0519	0.4874 \pm 0.0522
32	0.7986 \pm 0.0313	0.6417 \pm 0.0336	0.4509 \pm 0.0307	0.8468 \pm 0.0338	0.7127 \pm 0.0444	0.5309 \pm 0.0532
64	0.8245 \pm 0.0234	0.6873 \pm 0.0289	0.5018 \pm 0.0321	0.8568 \pm 0.0259	0.7374 \pm 0.0359	0.5674 \pm 0.0467
128	0.8387 \pm 0.0176	0.7187 \pm 0.0236	0.5446 \pm 0.0299	0.8611 \pm 0.0200	0.7533 \pm 0.0280	0.5937 \pm 0.0390
256	0.8472 \pm 0.0131	0.7391 \pm 0.0178	0.5788 \pm 0.0257	0.8632 \pm 0.0152	0.7630 \pm 0.0213	0.6144 \pm 0.0312
512	0.8522 \pm 0.0098	0.7527 \pm 0.0138	0.6053 \pm 0.0213	0.8638 \pm 0.0115	0.7694 \pm 0.0164	0.6304 \pm 0.0250
1024	0.8554 \pm 0.0075	0.7629 \pm 0.0107	0.6276 \pm 0.0162	0.8638 \pm 0.0089	0.7740 \pm 0.0121	0.6449 \pm 0.0189
2048	0.8582 \pm 0.0055	0.7709 \pm 0.0077	0.6443 \pm 0.0129	0.8642 \pm 0.0066	0.7786 \pm 0.0090	0.6558 \pm 0.0149
4096	0.8606 \pm 0.0043	0.7774 \pm 0.0061	0.6580 \pm 0.0097	0.8649 \pm 0.0051	0.7824 \pm 0.0068	0.6655 \pm 0.0110
8192	0.8627 \pm 0.0032	0.7826 \pm 0.0045	0.6694 \pm 0.0078	0.8657 \pm 0.0036	0.7859 \pm 0.0050	0.6470 \pm 0.0082
16384	0.8653 \pm 0.0025	0.7875 \pm 0.0037	0.6779 \pm 0.0054	0.8673 \pm 0.0026	0.7901 \pm 0.0042	0.6812 \pm 0.0057
32768	0.8676 \pm 0.0018	0.7919 \pm 0.0027	0.6861 \pm 0.0040	0.8690 \pm 0.0018	0.7937 \pm 0.0032	0.6884 \pm 0.0042
65536	0.8706 \pm 0.0015	0.7963 \pm 0.0020	0.6937 \pm 0.0022	0.8714 \pm 0.0017	0.7976 \pm 0.0024	0.6953 \pm 0.0025

^a Mean and $\pm 1\sigma$ realization-to-realization variation in porosity \mathcal{P} from eq. (12).

^b Mean and $\pm 1\sigma$ realization-to-realization variation in porosity P_{KBM} from eq. (14).

Prolate spheroids would have $b/a = 1$; oblate spheroids have $c/b = 1$. Figure 4 shows that the clusters are generally triaxial, with a tendency toward prolateness ($c/b > b/a$).

The ballistic aggregates constructed in this section are based on very simple algorithms. More realistic treatments of grain coagulation processes are possible (e.g., Ossenkopf 1993; Ormel et al. 2007), but are rather uncertain given our limited knowledge of the interstellar/circumstellar environment and grain properties. The well-defined sequence of BA to BAM2 clusters described here allows us to systematically investigate the grain properties as function of porosity.

4. Application of the Discrete Dipole Approximation

4.1. Composition

The composition of interstellar grains continues to be uncertain. The observed strength of the 10 μm absorption feature, produced by the Si-O stretching mode in silicates, requires that $\gtrsim 50\%$ of the total grain volume be amorphous silicate material. As discussed below, this amount of silicate material is also consistent with the observed depletions of Si, Mg, and Fe from the gas phase.

Attempts to reproduce the observed wavelength-dependent extinction require more grain material than can be provided by silicates alone (e.g., Weingartner & Draine 2001; Zubko et al. 2004). Because H_2O ice is not present in the diffuse interstellar medium, and Mg, Fe, and Si are presumed to be primarily invested in the silicate material, the only element that can provide substantial additional solid material is carbon. Observational evidence for carbonaceous material includes (see Draine 2003a, and references therein): (1) strong absorption near 0.22 μm , likely due to $\pi \rightarrow \pi^*$ electronic excitation in sp^2 -bonded carbon (e.g., graphite, or polycyclic aromatic hydrocarbons); (2) absorption at 3.4 μm (attributed to the C-H stretching mode); and (3) observed emission features at 3.3, 6.2, 7.6, 8.6, 11.3, and 12.7 μm that are attributed to vibrational modes of polycyclic aromatic hydrocarbons (PAHs). The cosmic abundance of carbon, and the fact that it is moderately depleted from the gas phase, is consistent with carbonaceous material with a total solid volume that is a substantial fraction of the volume of amorphous silicate material.

Assuming total interstellar abundances of the elements relative to H to be the same as current estimates of solar abundances, observations of gas-phase abundances in the interstellar medium allow us to infer the amount of different elements locked up in grains (see Table 1 of Draine 2008). Current estimates indicate that carbon in grains contributes a mass of about 0.13% of the total H mass, while solid material containing Mg, Fe, Si, O (plus small contributions from Al, Ca, and Ni) amounts to about 0.57% of the total H mass. If the carbonaceous material has a density of $\sim 2 \text{ g cm}^{-3}$, and the silicate material has a density $\sim 3.5 \text{ g cm}^{-3}$ then the overall silicate/carbon volume ratio is $V_{\text{sil}}/V_{\text{car}} \approx 2.5$. This, however, is based on assuming the total C abundance to be only 245 ± 30 ppm relative to H (Asplund et al. 2005b). However, two recent determinations of $(\text{O}/\text{H})_{\odot}$ (Landi et al. 2007; Centeno & Socas-Navarro 2008) obtain values that are ~ 1.9 times

larger than the solar oxygen abundance $(\text{O}/\text{H})_{\odot} = 457 \pm 56$ ppm of Asplund et al. (2004, 2005b). The solar C abundance might therefore be larger than Asplund et al.’s value of 245 ppm. If the total C abundance were to be increased to, e.g., 350 ppm, the mass of C in dust would increase by 75%, and the silicate/carbonaceous volume ratio would fall to $V_{\text{sil}}/V_{\text{car}} \approx 1.4$. The total abundances of Mg, Fe, Si – and therefore the inferred abundance of solids with silicate composition – are of course also uncertain. We conclude that if grains are of mixed composition, the silicate:carbonaceous volume fractions could be as large as 70:30, or as low as 60:40. We will consider extreme examples of composite grains that are 100% silicate, as well as composite grains with 50:50 volume fractions.

While the importance of carbon is undisputed, the specific form is uncertain. The observed PAH emission features require $\gtrsim 20\%$ of the solid carbon to be in small free-flying PAH molecules or clusters. Spectroscopy of the $3.4 \mu\text{m}$ feature indicates that $\sim 15\%$ of the hydrocarbon material is aliphatic (chain-like), and $\sim 85\%$ aromatic (sp^2 -bonded) (Pendleton & Allamandola 2002). Diamond (sp^3 -bonded carbon) has been found in meteorites, and may also be present in the interstellar medium, but there is no direct evidence for interstellar diamond.

Because the predominant form of carbon is uncertain, we consider two possibilities: crystalline graphite, and amorphous carbon. For graphite, a highly anisotropic material, we use the dielectric tensor from Draine (2003b). Each graphite sphere is assumed to be a single crystal, with the crystal axes for each graphite monomer assigned an independent random orientation.

“Amorphous carbon” is not a well-defined material, and its properties depend on the method of preparation. We use the dielectric function for amorphous carbon “AC1” from Rouleau & Martin (1991). For the amorphous silicate component, we use the “astrosilicate” dielectric function from Draine (2003b).

We will consider three compositions for the clusters: (1) 50% amorphous silicate and 50% graphite; (2) 50% amorphous silicate and 50% AC1; and (3) 100% amorphous silicate. For the mixed-composition clusters, the monomer compositions are assigned randomly, and the percentages are by volume.

4.2. DDA Method and Validity Criteria

We calculate the absorption and scattering properties of the BA, BAM1 and BAM2 clusters using DDSCAT 7.0 (Draine & Flatau 2008). DDSCAT is a code based on the discrete dipole approximation (Purcell & Pennypacker 1973; Draine & Flatau 1994), designed to compute scattering and absorption of electromagnetic waves by targets with arbitrary geometry and composition, for targets that are not too large compared to the wavelength λ .

There are three validity criteria that should be satisfied for the DDA to provide accurate results:

1. The interdipole spacing d should be small enough to resolve the geometric structure of the target. This is accomplished provided the number of dipoles per spherical monomer $n_{\text{dip}} \gtrsim 100$.
2. The phase shift corresponding to one dipole spacing should be small.

$$|m|kd = 0.44|m| \left(\frac{100}{n_{\text{dip}}} \right)^{1/3} \left(\frac{a_0}{0.02 \mu\text{m}} \right) \left(\frac{0.1 \mu\text{m}}{\lambda} \right) \lesssim 1 \quad (18)$$

where m is the refractive index, $k \equiv 2\pi/\lambda$, a_0 is the monomer sphere radius, and n_{dip} is the number of dipoles per sphere. Thus we see that $n_{\text{dip}} = 100$ allows condition (18) to be satisfied even at $\lambda = 0.1 \mu\text{m}$ for $a_0 = 0.02 \mu\text{m}$. For accurate calculations of the scattering phase function, the validity requirement is somewhat more stringent, $|m|kd \lesssim 0.5$. With $n_{\text{dip}} = 100$ and $a_0 = 0.02 \mu\text{m}$, we have $|m|kd \lesssim 0.5$ for $\lambda \gtrsim 0.2 \mu\text{m}$.

3. Even when the criterion $|m|kd < 0.5$ is satisfied, the implementation of the DDA used here overestimates absorption in materials with $\text{Im}(\epsilon) \gg 1$, where ϵ is the dielectric function. Graphite is a conducting material; the dielectric tensor component for $E \perp c$ (with c being the normal to the basal plane) becomes large in the infrared ($\epsilon_{\perp} = 11.7 + 32.6i$ at $\lambda = 3.981 \mu\text{m}$), and the accuracy of the DDA suffers.

To assess the computational accuracy, some of the scattering calculations have been repeated using differing numbers of dipoles per monomer n_{dip} . In the limit $n_{\text{dip}} \rightarrow \infty$, the DDA becomes exact. For finite n_{dip} , the errors are expected to scale as $n_{\text{dip}}^{-1/3}$ (i.e., the errors vary linearly with the interdipole separation d); such behavior has previously been demonstrated by Collinge & Draine (2004) and Yurkin et al. (2006).

Figure 5 shows the total extinction and scattering efficiencies computed for one cluster (50% silicate and 50% graphite) with $N = 256$ $a_0 = 0.02 \mu\text{m}$ monomers, and porosity $\mathcal{P} = 0.853$, for a single orientation, using different numbers of dipoles with $n_{\text{dip}} \approx 100, 200, 400, 1000$. The results show that the computed cross sections at each wavelength are approximately linear functions of $n_{\text{dip}}^{-1/3}$, allowing us to confidently extrapolate to estimate the exact result at $n_{\text{dip}}^{-1/3} \rightarrow 0$, and thereby to estimate the error that would result if we were to simply use cross sections calculated for $n_{\text{dip}} \approx 100$. On average, the fractional errors for the results with $n_{\text{dip}} \approx 100$ are only a few percent for $\lambda \lesssim 0.35 \mu\text{m}$, 4–10% for $0.35 < \lambda < 0.8 \mu\text{m}$, and 10–15% for $0.8 < \lambda < 4 \mu\text{m}$. Note that for wavelengths $\lambda \gtrsim 0.5 \mu\text{m}$, the computations for finite n_{dip} always *overestimate* the absorption cross section and scattering cross sections, presumably as a result of failure to accurately resolve the “shielding” produced by the charge layer produced by the discontinuity in the polarization field at the grain surface.

⁴At $\lambda = 0.1 \mu\text{m}$, $|m| = 1.84, 2.41, 2.15, 1.91$ for astrosilicate, graphite with $E \perp c$, graphite with $E \parallel c$, and AC1.

The fractional errors of $\sim 10\%$ in the infrared are comparable to the typical variations in Q_{abs} and Q_{ext} from one random realization to another. Hence using $n_{\text{dip}} \approx 100$ dipoles per monomer suffices for most of our investigations⁵, and allows us to explore the parameter space more efficiently.

For the DDA results presented in the next section, each calculation is averaged over a few (3 or 5) realizations and 54 random orientations for each realization. The typical variations in cross sections from realization to realization for the same type of clusters are of the order $\lesssim 10\%$; while 54 random orientations are sufficient to represent the orientational average (see Johnson & Draine 2008). The scattering and absorption are calculated at 32 wavelengths from 0.1 to 3.981 μm (with $\Delta \log_{10} \lambda = 0.05, 0.025, 0.05, 0.1$ for $0.1 \leq \lambda \leq 0.1259, 0.1259 < \lambda \leq 0.3126, 0.3126 < \lambda \leq 0.5012$ and $0.5012 < \lambda \leq 3.981 \mu\text{m}$, respectively).

5. Absorption, Scattering, and Extinction Cross Sections of Aggregates

In §§5.1,5.2 we fix the effective radius $a_{\text{eff}} = 0.127 \mu\text{m}$ for each cluster and explore the differences in optical properties between three different cluster geometries and three different compositions. The aggregates have characteristic radius $R_{abc} \approx 0.16\text{--}0.24 \mu\text{m}$. In §5.2 we vary the monomer size to investigate the sensitivity of results to monomer size and to porosity at fixed a_{eff} . In §5.3 we compare our DDA results with the analytical multi-layer sphere model (Voshchinnikov & Mathis 1999) to test the accuracy of the MLS prescription for estimating the optical properties of ballistic aggregates. In §5.4 we carry out a similar comparison of our DDA results with “effective medium theory”.

5.1. DDA Results: Dependence on Wavelength and Porosity

The orientation- and realization-averaged (5 realizations) extinction cross section, absorption cross section and scattering cross section, as well as the asymmetry parameter $g \equiv \langle \cos \theta \rangle$ are plotted in Figure 6, for the three aggregate types (BA, BAM1, BAM2) and three different compositions, as functions of wavelength. We have used the results computed with $n_{\text{dip}} \approx 400$, which are within a few percent of the exact values as inferred from Fig. 5.

For wavelength $\lambda \gg a_{\text{eff}}$, the clusters are in the Rayleigh limit; the extinction is dominated by absorption, and the asymmetry parameter $g \equiv \langle \cos \theta \rangle$ is small. For the same volume of solid material, the 100% silicate clusters have smaller absorption (and therefore total extinction) at long wavelength, because graphite and AC1 are more absorptive than silicate in the near-infrared. At short wavelength, the behavior of the cross sections and g is nonmonotonic. For example, for the 50% silicate/50% graphite clusters, Q_{ext} has a dip at $\sim 0.17 \mu\text{m}$ and peak near $0.22 \mu\text{m}$.

⁵ For clusters with $N \leq 512$, we use results obtained with $n_{\text{dip}} \approx 400$ for improved accuracy; for larger clusters, i.e., $N = 1024, 2048$, etc., we use $n_{\text{dip}} \approx 100$ due to computational limits.

An important question is how the porosity of the dust grain affects the extinction efficiency. One might expect that increased porosity would lead to an increase in the overall extinction cross section per unit solid material, which motivated attempts to try to use porous dust grains to circumvent the difficulties in accounting for the observed interstellar extinction without overconsuming the elements used to build grains. Fig. 6 shows that for short wavelengths, increased porosity does result in a modest increase in extinction. However, this effect reverses longward of a transition wavelength λ_t . The transition wavelength $\lambda_t \sim 0.34 \mu\text{m}$ for 50% silicate/50% graphite, $\sim 0.25 \mu\text{m}$ for 50% silicate/50% AC1, and $\sim 0.20 \mu\text{m}$ for 100% silicate. For these three examples, $\lambda_t \approx (2.1 \pm 0.6)a_{\text{eff}}$.

Although in this section we focused on clusters with $a_{\text{eff}} = 0.127 \mu\text{m}$, similar behavior is seen for other cluster sizes. The transition wavelength at which the effect of porosity reverses increases when the overall size of aggregate clusters increases. Based on limited numerical experiments, we conjecture that, in general, the transition wavelength occurs at $\lambda_t \approx (2.5 \pm 1.0)a_{\text{eff}}$: porosity appears to increase the extinction cross section per unit solid material for $\lambda \lesssim 1.5a_{\text{eff}}$, while *reducing* the extinction per unit solid material at $\lambda \gtrsim 3.5a_{\text{eff}}$.

It is interesting to note that for the 50% silicate/50% AC1 case, similar trends are seen in Voshchinnikov et al. (2006, fig. 2), where the porous dust grain is spherical and modeled using the EMT-Mie theory. The fact that porosity actually decreases the extinction efficiency at $\lambda > \lambda_t \approx 2a_{\text{eff}}$ was also seen by West (1991), who used two types of aggregates with different porosity and compared with the results of equal-volume spheres, and found that porosity caused a decrease in extinction efficiency when the equivalent size parameter is $2\pi R/\lambda \leq 5$ (i.e., fig. 3 in West 1991).

5.2. Effects of monomer size/sensitivity to porosity

In the above discussion, we fixed the monomer size to be 200 \AA in radius. There is no direct evidence of how large the monomers should be, hence we need to know if different monomer size inside a ballistic aggregate will affect the overall absorption and scattering cross sections. To this end, we choose two different monomer sizes, 100 \AA and 400 \AA , for the BAM2 clusters with 2048 monomers and 32 monomers respectively. These results will be compared with our fiducial BAM2 clusters with $256 a_0 = 200 \text{ \AA}$ monomers discussed in §5.1: we are comparing three clusters with the same a_{eff} , i.e., composed of the same amount of solid materials. We focus on the 50% silicate/50% graphite case. For every cluster we average over three realizations, and many random orientations of each realization. We used $n_{\text{dip}} \sim 100$ for the 2048-monomer clusters and $n_{\text{dip}} \sim 400$ for the 256-monomer and 32-monomer clusters. To satisfy the DDA accuracy criterion equation (18) we only focus on results with wavelength $\lambda \geq 0.2 \mu\text{m}$. We note that although the three clusters contain identical volumes of solid materials with $a_{\text{eff}} = 0.127 \mu\text{m}$, the porosity is different for the 32, 256, 2048 clusters, with $\mathcal{P} \approx 0.45, 0.58, \text{ and } 0.64$, respectively.

We show the results in Fig. 7, for $Q_{\text{ext}}, Q_{\text{abs}}, Q_{\text{sca}}$ and $g \equiv \langle \cos \theta \rangle$ respectively. Since the

three clusters have same amount of solid materials but different porosity (porosity increases with increasing number of monomers), this behavior is very similar to the general behavior of BA, BAM1 and BAM2 clusters as shown in Fig. 6. Once again, there is a “transition” wavelength $\lambda_t \approx 3a_{\text{eff}}$ where the calculated Q_{ext} is approximately independent of \mathcal{P} (the $a_{\text{eff}} = 0.127 \mu\text{m}$ clusters in Fig. 6 have $\lambda_t \approx 0.34 \mu\text{m} \approx 2.7a_{\text{eff}}$, and the $a_{\text{eff}} = 0.127 \mu\text{m}$ clusters in Fig. 7 have $\lambda_t \approx 0.42 \mu\text{m} \approx 3.3a_{\text{eff}}$).

Although in Fig. 7 there seems to be a second transition wavelength at $\sim 1.5 \mu\text{m}$, we caution that it might be artificial because the accuracy of our DDA results decreases at the longest wavelengths (see Fig. 5) for small n_{dip} . This is particularly true for the 2048 case where we used $n_{\text{dip}} \approx 100$ due to computational limits.

To further demonstrate that the effect seen in Fig. 7 is actually the result of varying the porosity, we carry out another test. In Figure 8 we compare two clusters with different geometries (BAM1 vs. BAM2), and different monomer sizes (504 \AA vs. 200 \AA), but with the same amount of material ($a_{\text{eff}} = 0.160 \mu\text{m}$), and approximately the same porosity ($\mathcal{P} \approx 0.62$). The two clusters have very similar cross sections for extinction, absorption, and scattering. Thus we conclude that the important parameters are just a_{eff} (i.e., the amount of solid material) and the porosity \mathcal{P} , and monomer size does not have significant effects as long as the monomer size $a_0 \lesssim \lambda/2\pi$.

5.3. Comparison with the MLS Approximation

The DDA computations described above are very time-consuming. To model porous, composite dust grains, some authors have used the analytical multi-layer sphere (MLS) model (Voshchinnikov & Mathis 1999; Voshchinnikov et al. 2005, 2006), where the sphere is composed of concentric spherical shells, each of which is further composed of a set of spherical layers of single composition. The number of such shells should be large enough so that the results are unaffected by changing the order of layers inside each shell; in other words, the materials are well-mixed inside such spheres. The problem of light scattering and absorption by a multi-layer sphere can be solved by a fast algorithm (e.g., Wu et al. 1997). The applicability of the MLS model to the aggregates considered here has not previously been examined.

To compare the DDA results with the MLS model, one needs to know the vacuum fraction f_{vac} , which is the volume fraction of vacuum in the multi-layer sphere. Proponents of the MLS method have not addressed the question of what value to use for f_{vac} when modeling random aggregates; the optimal value of f_{vac} is not necessarily equal to the porosity \mathcal{P} given by eq. (12). Therefore we test the MLS using different values of f_{vac} to find the value of f_{vac} that minimizes the difference between the DDA results and the MLS results. In practice we set $f_{\text{vac}} = 0.1 - 0.9$ with an increment of $\Delta f_{\text{vac}} = 0.1$ in the MLS calculations. We set the number of shells in the MLS to be 40 so that the results do not vary significantly when the order of layers inside each shell is changed.

We plot the results of MLS calculations on top of the DDA results in Fig. 6 as black lines, which are bounded by the black dashed line with $f_{\text{vac}} = 0.1$ and the black dotted line with $f_{\text{vac}} = 0.9$. MLS

results using intermediate vacuum fractions lie between these two bounds. One can immediately see that the MLS model is not a good approximation, especially for the 50% silicate/50% graphite case. For the 50% silicate/50% AC1 case, the MLS results have two transition wavelengths ($\sim 0.31 \mu\text{m}$ and $\sim 0.95 \mu\text{m}$) at which the effect of porosity reverses, as has already been reported by Voshchinnikov et al. (2006), although $a_{\text{eff}} = 0.1 \mu\text{m}$ in their work and $0.127 \mu\text{m}$ here. However, this is different from our DDA results where there is only one transition wavelength, near $\sim 0.25 \mu\text{m}$. Similar results are found for the 100% silicate case. For the 50% silicate/50% graphite case the MLS model fails to predict such a transition altogether – increasing the porosity increases the MLS extinction at all wavelengths between 0.1 and $4 \mu\text{m}$. For all three compositions, the MLS model seems to underestimate the extinction at short wavelengths and overestimate the extinction at long wavelengths. Our DDA results are of limited accuracy (errors of up to $\sim 8\%$) at long wavelengths for $n_{\text{dip}} \approx 400$ (see Fig. 5), but the exact extinction values are even lower at these wavelengths, hence the MLS errors are even larger than shown in Fig. 6.

To quantify the deviation of the MLS results from the DDA results we define a global error averaged over all 32 wavelengths:

$$(\text{global error } Q_x)^2 = \langle [\ln(Q_{x,\text{MLS}}/Q_{x,\text{DDA}})]^2 \rangle . \quad (19)$$

Fig. 9 shows the global errors of Q_{ext} , Q_{abs} , and Q_{sca} for the three types of aggregates and three compositions, averaged over 5 realizations. Dotted lines show the standard deviation from the 5 realizations. It is clear that the accuracy of the MLS model decreases when the porosity increases (from BAM2 to BA clusters) or when the constituent materials become more absorptive (from 100% silicate to 50% silicate/50% graphite).

5.4. Comparison with the EMT Approximation

One approach to estimate the optical properties of random aggregates is to approximate them by homogeneous spheres, with an “effective” refractive index obtained from “effective medium theory” (EMT); the scattering and absorption by the homogeneous sphere is then calculated using Mie theory. Effective medium theory comes in more than one variant; here we consider the form of EMT developed by Bruggeman (see Bohren & Huffman 1983) where the effective dielectric permittivity ϵ_{eff} is calculated via

$$\sum_i f_i \frac{\epsilon_i - \epsilon_{\text{eff}}}{\epsilon_i + 2\epsilon_{\text{eff}}} = 0 , \quad (20)$$

where f_i and ϵ_i are the volume fraction and dielectric permittivity of each composition, including vacuum. Note that ϵ_{eff} calculated in this way is not affected by the detailed structure of the composite grain, i.e., “monomer size” does not matter. If the aggregate contains n distinct materials (including vacuum), then ϵ_{eff} is a root of an n^{th} order complex polynomial equation. We find that there is always just one root with $\text{Im}(\epsilon_{\text{eff}}) \geq 0$ – this is the physically meaningful solution.

The cross sections calculated using EMT are compared to the DDA results in Fig. 10 using our fiducial $N = 256$ clusters with $a_0 = 0.02 \mu\text{m}$, and the global errors from the EMT approximation are shown in Fig. 11. We take the vacuum fraction in the EMT-Mie model to be $f_{\text{vac}} = 0.1 - 0.9$ with $\Delta f_{\text{vac}} = 0.05$. The EMT-Mie approach provides much better agreements with the DDA results than the MLS approximation does. This is particularly true for the silicate-graphite and the silicate-AC1 compositions, where one material is highly absorptive. It is clear from Figs. 6 and 10 that the difference between MLS and EMT-Mie increases when f_{vac} increases, which is also evident in fig. 2 of Voshchinnikov et al. (2006) for the silicate-AC1 case. Our ballistic aggregates have porosities $\mathcal{P} \gtrsim 0.6$, hence it is not surprising that the MLS model is not a good approximation.

The global error plots in Fig. 11 show that the EMT-Mie model gives the optimal results when⁶ $f_{\text{vac}} = 0.80, 0.70, 0.55$ for BA, BAM1, BAM2 clusters respectively: it appears that for the three types of aggregates the optimal vacuum fraction for EMT-Mie calculations is

$$f_{\text{vac}} \approx 0.94\mathcal{P} . \quad (21)$$

The global errors of Q_{ext} etc. are $\lesssim 10\%$ at this optimal f_{vac} , which suggests that the EMT-Mie model provides a fairly good approximation for computing overall cross sections. We plot the difference between the EMT-Mie results (for optimal choice of f_{vac}) and the DDA results, as functions of wavelength, in Fig. 12. It shows that although the EMT-Mie results do not follow the DDA results exactly, the maximum deviations are typically $\sim 20\%$ in all cases. It is also apparent that the EMT-Mie model produces more forward scattering at short wavelength, a property that is further discussed in Paper II, which examines the angular distribution and polarization of the scattered light.

6. Summary and Discussions

The principal results of this study are the following:

1. Two new algorithms for generating random aggregates are introduced: ballistic aggregation with one migration (BAM1), and ballistic aggregation with two migrations (BAM2). BAM1 and BAM2 aggregates are less porous, and more mechanically robust, than conventional BA aggregates.
2. A measure \mathcal{P} of the porosity of a structure is proposed (eq. 10), as well as a measure R_{abc} (eq. 11) for the “characteristic size” of the structure.
3. Monte-Carlo simulations are used to determine the statistical properties of \mathcal{P} and R_{abc} for ballistic aggregates (see Tables 1-2 and Figs. 2-3).

⁶These are not the exact values of porosity at which the EMT-Mie model fits the DDA results best, because our grid of vacuum fraction has a coarse grid size of $\Delta f_{\text{vac}} = 0.05$.

4. We confirm (see Figure 5) that the accuracy of the DDA scales as the interdipole spacing d as $d \rightarrow 0$, or, equivalently as $N_{\text{dip}}^{-1/3}$ as $N_{\text{dip}} \rightarrow \infty$, where N_{dip} is the total number of dipoles.
5. Scattering, absorption, and extinction cross sections are calculated for the $N = 256$, $a_0 = 0.02 \mu\text{m}$ ($a_{\text{eff}} = 0.127 \mu\text{m}$) BA, BAM1, and BAM2 clusters, for three different compositions: 100% silicate, 50% silicate/50% amorphous carbon, and 50% silicate/50% graphite, for wavelengths $0.1 \leq \lambda \leq 3.981 \mu\text{m}$. The BA clusters (with the highest porosity \mathcal{P}) have the largest extinction cross sections at short wavelengths, but at optical and near-IR wavelengths, the BAM2 clusters (with the lowest \mathcal{P}) provide more extinction per unit solid material. At constant porosity and same amount of solid material, the monomer size has no significant effect provided the monomers are small compared to the incident wavelength.
6. We compared the DDA results with the analytical MLS model and EMT-Mie theory. We found the MLS model does not provide a good approximation for absorptive and/or very porous grains; the EMT-Mie model provides much better agreement with the DDA results. For computing total cross sections (Q_{ext} , Q_{abs} , Q_{sca}), the EMT-Mie method provides results accurate to $\sim 10\%$ if the vacuum fraction f_{vac} is taken to be $0.94\mathcal{P}$.

The effects of porosity on extinction cross sections have important implications for the abundance budget problem in interstellar dust models. The recent observed decrease of solar abundances (e.g., Asplund et al. 2005a) and the claim that interstellar abundances might be better represented by those of B stars (e.g., Snow & Witt 1996) have imposed a challenge to dust extinction models. Porous dust grains have been thought to be a solution to this abundance budget problem (e.g., Mathis 1996), because they were expected to result in greater extinction per unit solid material than compact grains. However, our results show that porosity actually *decreases* the opacity at wavelengths long compared to the overall grain size. Hence caution must be paid when dealing with the abundance budget problem. Until detailed models have been constructed using random aggregates to reproduce the observed interstellar extinction (and polarization), we will not know if such grain models will alleviate the interstellar abundance problem. Work on this problem is underway (Johnson & Draine 2008).

Ballistic aggregates are promising candidates for interstellar and circumstellar dust grains. In the companion Paper II, we will discuss the scattering properties of ballistic aggregates and present examples that can reproduce the observations of light scattered by dust in debris disks and comets.

We thank the anonymous referee for helpful comments. This research was supported in part by NSF grant AST-0406883. Computations were performed on the Della and Artemis computer clusters at Princeton University.

REFERENCES

- Asano, S., & Sato, M. 1980, *Appl. Opt.*, 19, 962
- Asano, S., & Yamamoto, G. 1975, *Appl. Opt.*, 14, 29
- Asplund, M., Grevesse, N., & Sauval, A. J. 2005a, in *ASP Conf. Ser. 336: Cosmic Abundances as Records of Stellar Evolution and Nucleosynthesis*, ed. T. G. Barnes, III & F. N. Bash, 25–+
- Asplund, M., Grevesse, N., Sauval, A. J., Allende Prieto, C., & Blomme, R. 2005b, *A&A*, 431, 693
- Asplund, M., Grevesse, N., Sauval, A. J., Allende Prieto, C., & Kiselman, D. 2004, *A&A*, 417, 751
- Bertini, I., Thomas, N., & Barbieri, C. 2007, *A&A*, 461, 351
- Blum, J., & Wurm, G. 2000, *Icarus*, 143, 138
- Bohren, C. F., & Huffman, D. R. 1983, *Absorption and Scattering of Light by Small Particles* (New York: Wiley)
- Brownlee, D. E. 1985, *Annual Review of Earth and Planetary Sciences*, 13, 147
- Centeno, R., & Socas-Navarro, H. 2008, *ApJ*, 682, L61
- Collinge, M. J., & Draine, B. T. 2004, *J. Opt. Soc. Am.*, 21, 2023
- Dorschner, J., & Henning, T. 1995, *A&A Rev.*, 6, 271
- Draine, B. T. 2003a, *ARA&A*, 41, 241
- . 2003b, *ApJ*, 598, 1017
- . 2008, *Space Science Reviews*, 000, 000
- Draine, B. T., & Flatau, P. 1994, *J. Opt. Soc. Am.*, 11, 1491
- . 2008, *ArXiv Astrophysics e-prints*
- Farafonov, V. G., Voshchinnikov, N. V., & Somsikov, V. V. 1996, *Appl. Opt.*, 35, 5412
- Johnson, E. T., & Draine, B. T. 2008, *ApJ*, in preparation, 000, 000
- Kimura, H., Kolokolova, L., & Mann, I. 2006, *A&A*, 449, 1243
- Kozasa, T., Blum, J., & Mukai, T. 1992, *A&A*, 263, 423
- Kozasa, T., Blum, J., Okamoto, H., & Mukai, T. 1993, *A&A*, 276, 278
- Krause, M., & Blum, J. 2004, *Phys. Rev. Lett.*, 93, 021103

- Landi, E., Feldman, U., & Doschek, G. A. 2007, *ApJ*, 659, 743
- Li, A., & Greenberg, J. M. 1998, *A&A*, 331, 291
- Lumme, K., & Rahola, J. 1994, *ApJ*, 425, 653
- Mackowski, D. W. 1991, *Proc. Royal Soc. London Ser A*, 433, 599
- Mackowski, D. W., & Mishchenko, M. I. 1996, *J. Opt. Soc. Am.*, 13, 2266
- Mathis, J. S. 1996, *ApJ*, 472, 643
- Mathis, J. S., & Whiffen, G. 1989, *ApJ*, 341, 808
- Mishchenko, M. I., & Travis, L. D. 1994, *Opt. Comm.*, 109, 16
- Nakamura, R., Kitada, Y., & Mukai, T. 1994, *Planet. Space Sci.*, 42, 721
- Ormel, C. W., Spaans, M., & Tielens, A. G. G. M. 2007, *A&A*, 461, 215
- Ossenkopf, V. 1993, *A&A*, 280, 617
- Pendleton, Y. J., & Allamandola, L. J. 2002, *ApJS*, 138, 75
- Petrova, E. V., Jockers, K., & Kiselev, N. N. 2000, *Icarus*, 148, 526
- Purcell, E. M., & Pennypacker, C. R. 1973, *ApJ*, 186, 705
- Rouleau, F., & Martin, P. G. 1991, *ApJ*, 377, 526
- Shen, Y., Draine, B. T., & Johnson, E. T. 2007, in preparation
- Snow, T. P., & Witt, A. N. 1996, *ApJ*, 468, L65
- Voshchinnikov, N. V., & Farafonov, V. G. 1993, *Ap&SS*, 204, 19
- Voshchinnikov, N. V., Il'in, V. B., & Henning, T. 2005, *A&A*, 429, 371
- Voshchinnikov, N. V., Il'in, V. B., Henning, T., & Dubkova, D. N. 2006, *A&A*, 445, 167
- Voshchinnikov, N. V., & Mathis, J. S. 1999, *ApJ*, 526, 257
- Warren, J. L., Barrett, R. A., Dodson, A. L., Watts, L. A., & Zolensky, M. E. 1994, *Cosmic Dust Catalog*, 14
- Waterman, P. C. 1971, *Phys. Rev. D*, 3, 825
- Weingartner, J. C., & Draine, B. T. 2001, *ApJ*, 548, 296
- West, R. A. 1991, *Appl. Opt.*, 30, 5316

- Wielgaard, D. J., Mishchenko, M. I., Macke, A., & Carlson, B. E. 1997, *Appl. Opt.*, 36, 4305
- Witten, T. A., & Cates, M. E. 1986, *Science*, 232, 1607
- Wu, Z., Guo, L. X., Ren, K. F., Gouesbet, G., & Gréhan, G. 1997, *Appl. Opt.*, 36, 5188
- Wurm, G., & Blum, J. 1998, *Icarus*, 132, 125
- Xu, Y.-L. 1997, *Appl. Opt.*, 36, 9496
- Yurkin, M. A., Maltsev, V. P., & Hoekstra, A. G. 2006, *J. Opt. Soc. Am.*, 23, 2578
- Zubko, V., Dwek, E., & Arendt, R. G. 2004, *ApJS*, 152, 211

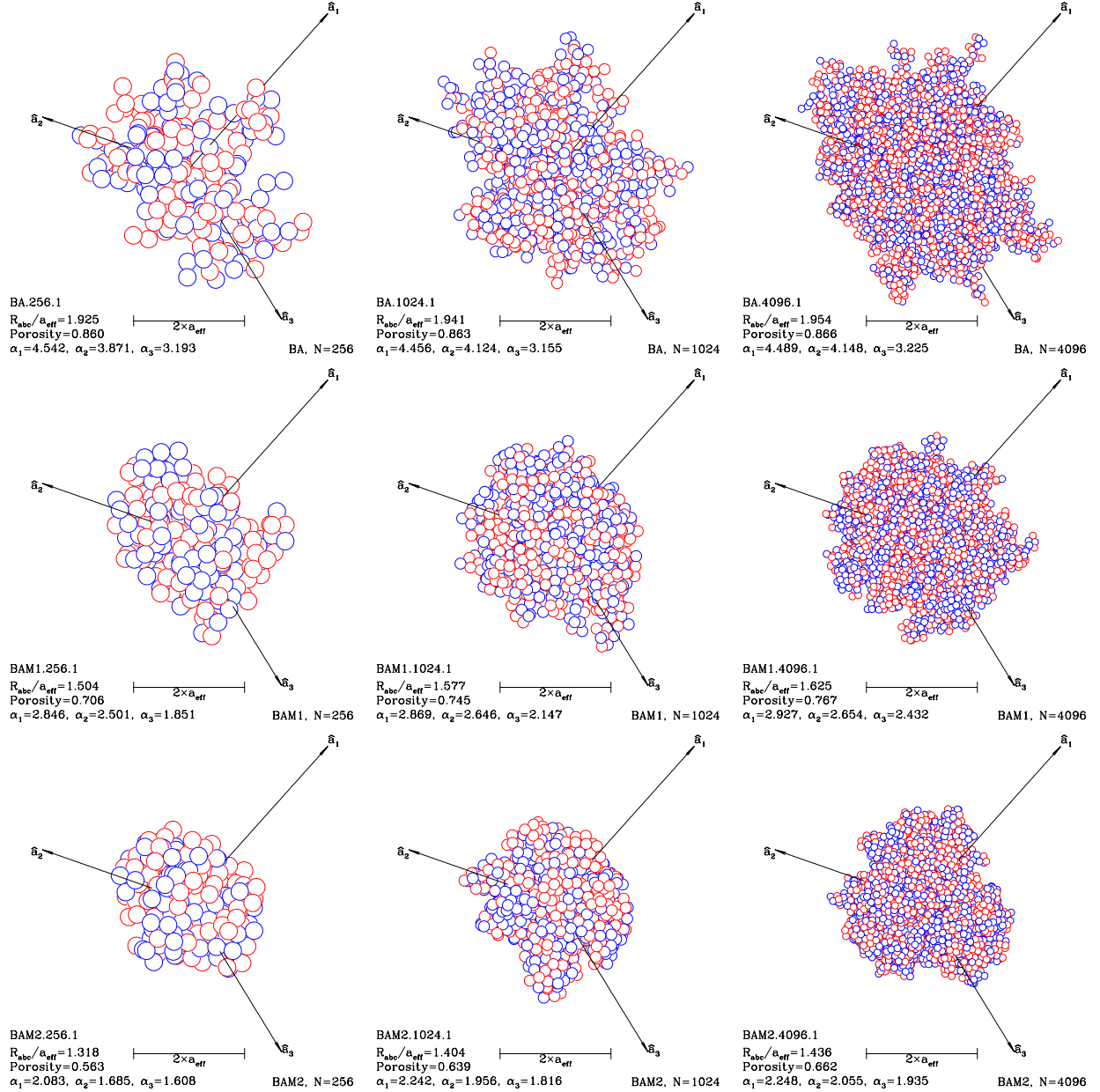


Fig. 1.— From left to right: $N=256$, 1024 , and 4096 clusters. From top to bottom: BA, BAM1, and BAM2 aggregation rules. Axes \hat{a}_1 , \hat{a}_2 , \hat{a}_3 are the principal axes with the largest, intermediate, and smallest moment of inertia. For each cluster we give the characteristic radius R_{abc} , the porosity \mathcal{P} , and the dimensionless moment-of-inertia eigenvalues α_i .

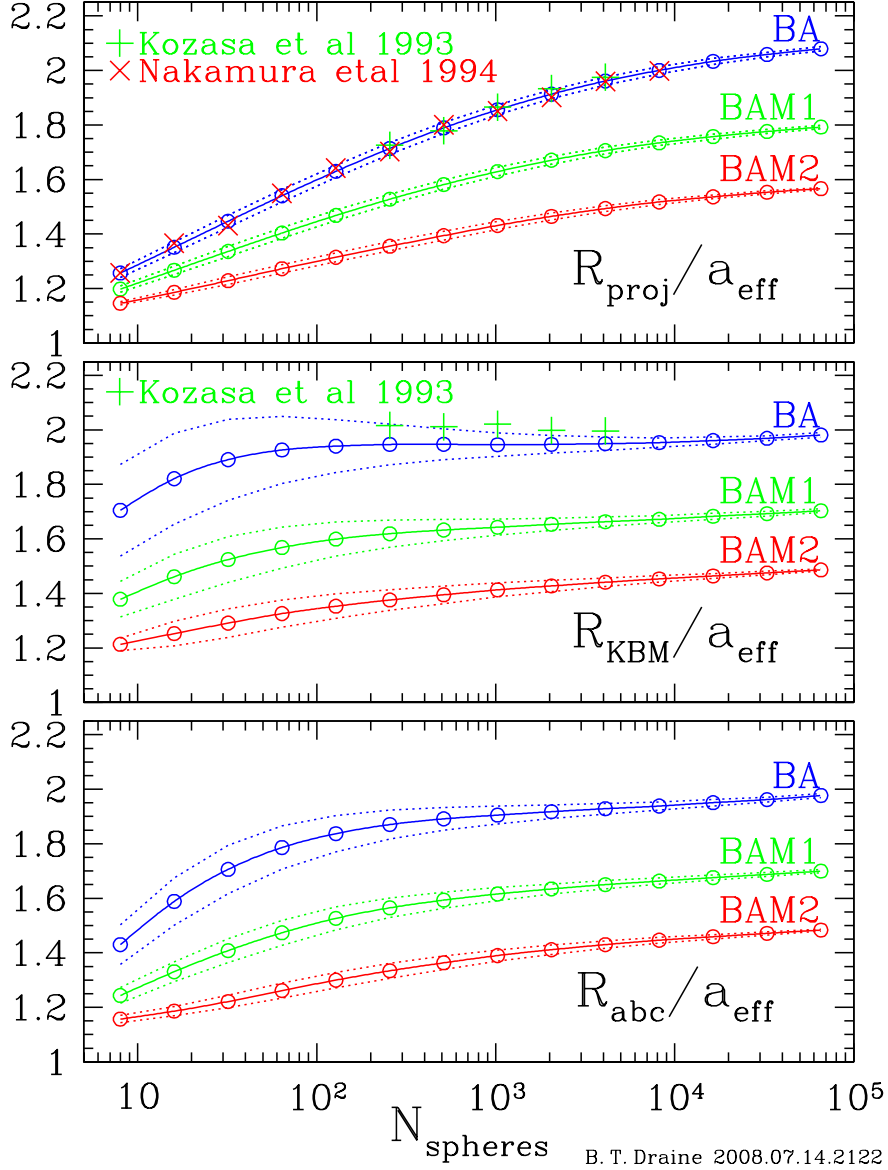


Fig. 2.— Characteristic radius R_{abc} , R_{KBM} , and the radius R_{proj} based on mean projected area, for clusters produced by BA, BAM1, and BAM2 aggregation rules with single-size spheres (see text). Solid lines connect the mean values. Dotted lines show the $\pm 1\sigma$ dispersion for random realizations. For BA clusters, we show R_{KBM} and R_{proj} reported by Kozasa et al. (1993), and R_{proj} given by Nakamura et al. (1994).

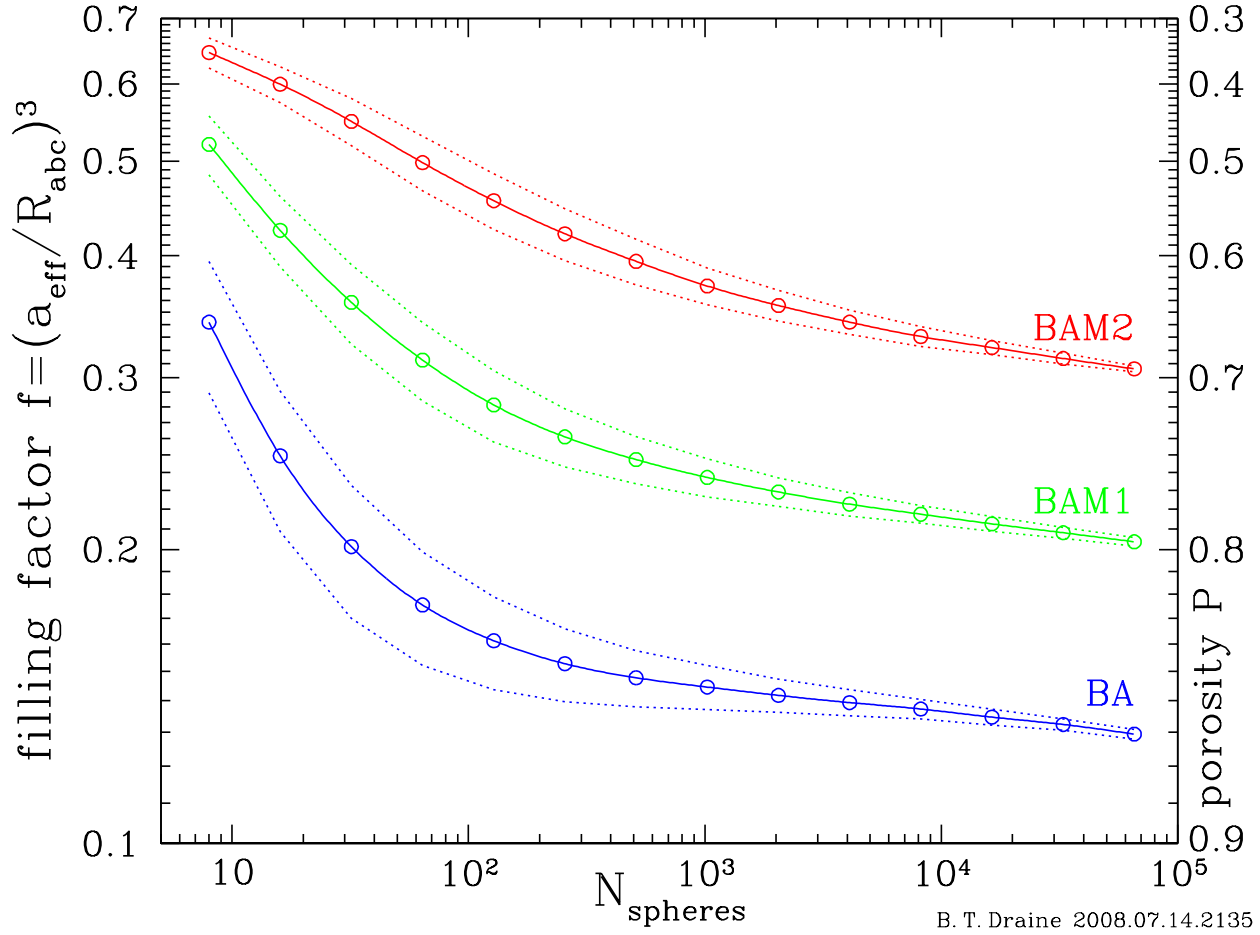


Fig. 3.— Volume filling factor f (left scale) and porosity \mathcal{P} (right scale) for clusters produced by BA, BAM1, or BAM2 aggregation rules with single-size spheres. Solid lines connect the mean values. Dotted lines show the $\pm 1\sigma$ dispersion for random realizations. BA clusters are the least dense, with porosity $\mathcal{P} \approx 0.87$ in the limit $N \rightarrow \infty$. BAM2 clusters are the most dense, with $\mathcal{P} \approx 0.70$ in the limit $N \rightarrow \infty$.

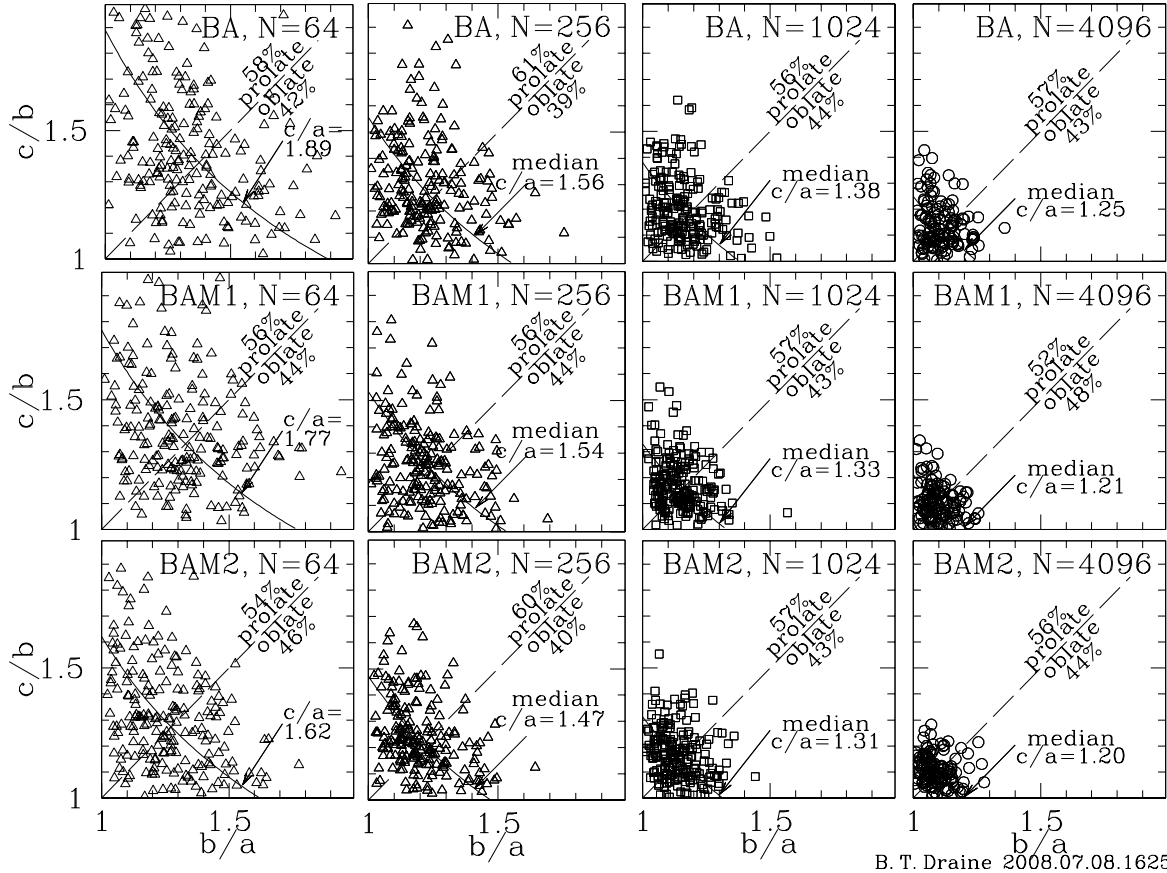


Fig. 4.— Axial ratios for BA, BAM1, and BAM2 clusters of N spheres, for $N = 64, 256, 1024,$ and 4096 . BA clusters are more asymmetric than BAM1 clusters, which in turn are more asymmetric than BAM2 clusters. Prolate shapes ($c/b > b/a$) appear to be slightly favored, and there is an overall tendency for clusters to be rounder as N increases.

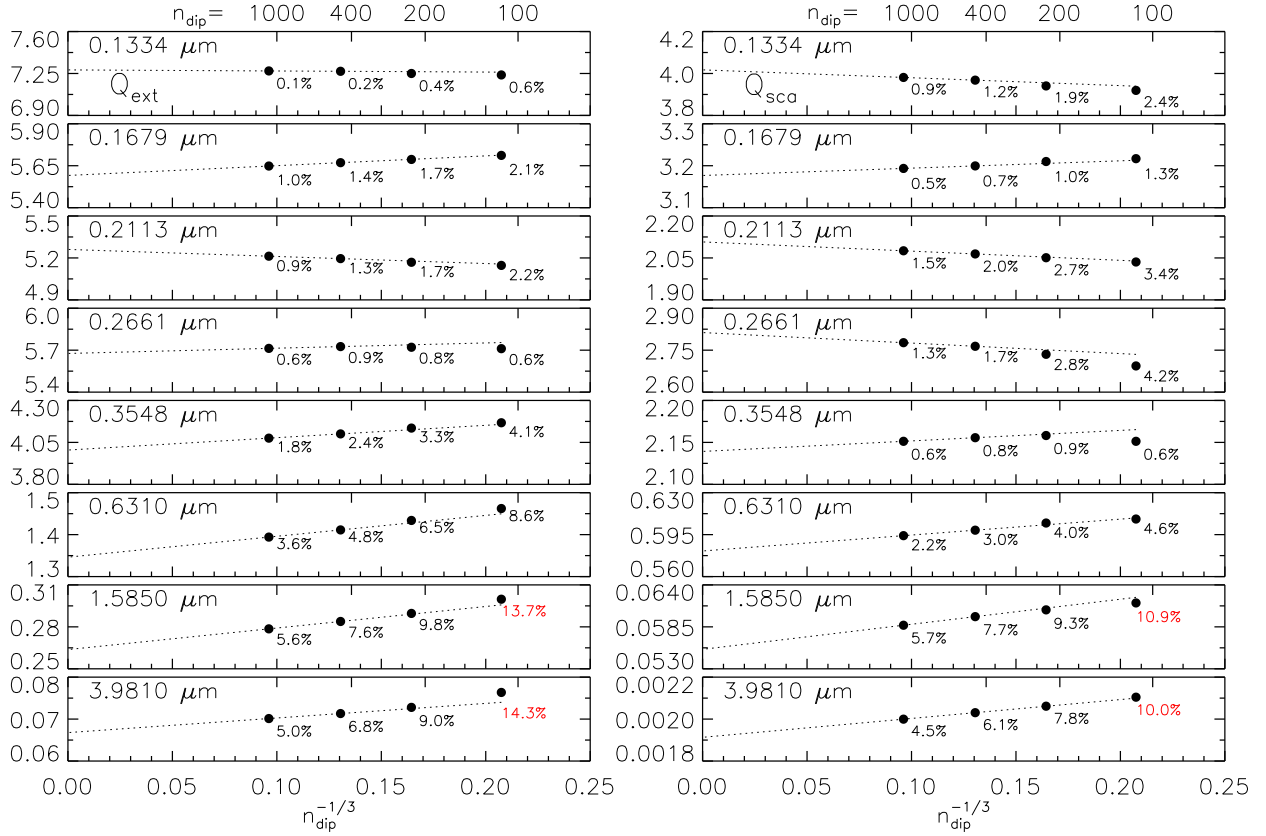


Fig. 5.— Convergence tests for the DDA method. Shown here are the extinction (left) and scattering (right) efficiencies for one $N = 256$, $a_0 = 0.02 \mu\text{m}$, 50% silicate and 50% graphite cluster with $\mathcal{P} = 0.853$, computed using $n_{\text{dip}} \approx 100, 200, 400, 1000$, for selected wavelengths (as marked on top-left of each panel, in units of μm), and for a single orientation. The filled circles are the results, and the dotted lines are extrapolations to $n_{\text{dip}} \rightarrow \infty$ using the $n_{\text{dip}} \approx 400$ and 1000 results (see text). The percentage alongside each data point is the fractional error with respect to the extrapolated value at $n_{\text{dip}} \rightarrow \infty$.

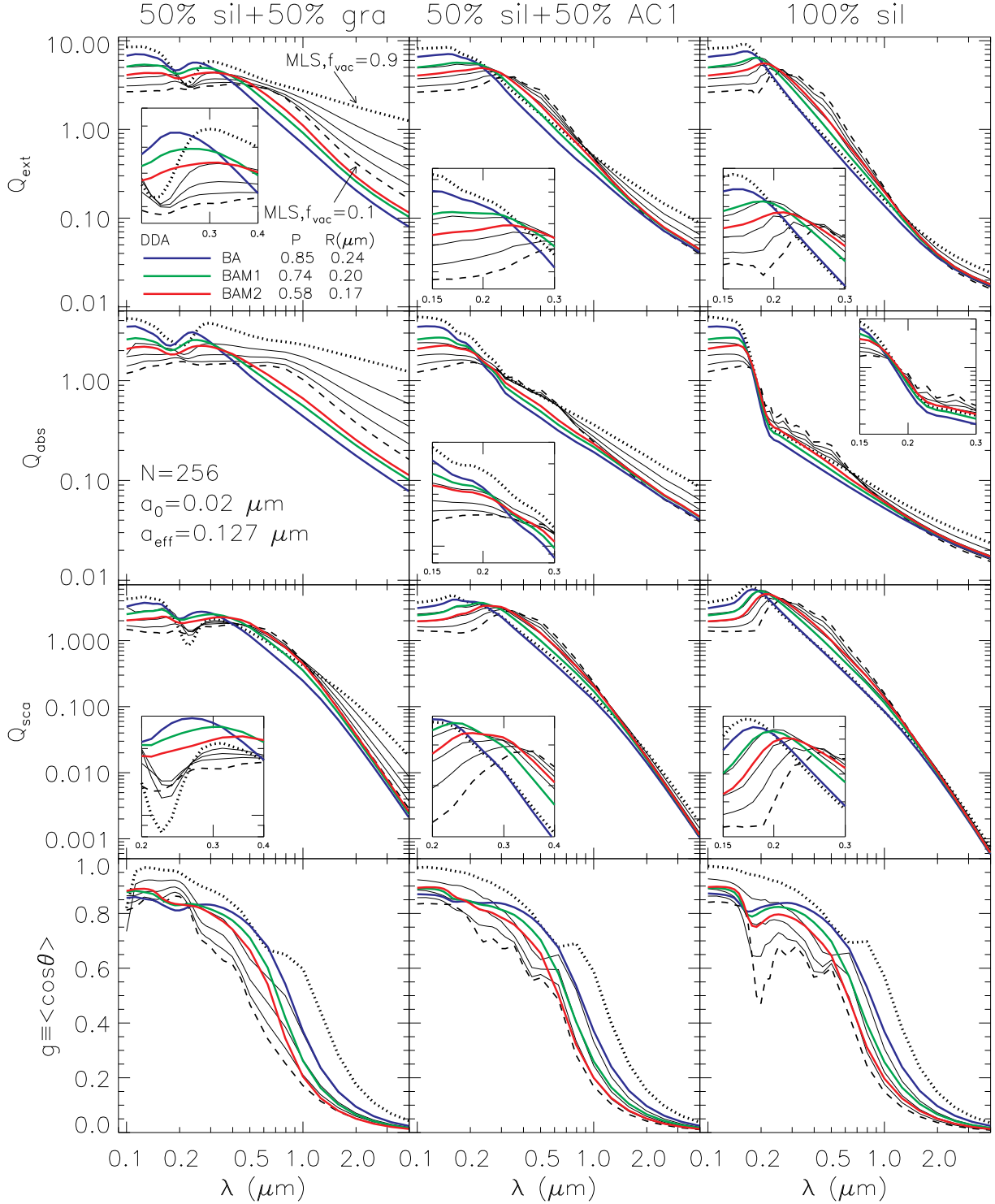


Fig. 6.— Wavelength dependence of orientation-averaged Q_{ext} , Q_{abs} , Q_{sca} and $g \equiv \langle \cos \theta \rangle$ for three compositions and three aggregate types, for the fiducial $N = 256$ and $a_0 = 0.02 \mu\text{m}$ clusters with $n_{\text{dip}} \approx 400$. Each type of cluster is averaged over 5 realizations. Also plotted are the results of the MLS model: the black dashed lines are the MLS results with $f_{\text{vac}} = 0.1$, the black dotted lines are for $f_{\text{vac}} = 0.9$, and the black solid lines are for $f_{\text{vac}} = 0.3, 0.5, 0.7$.

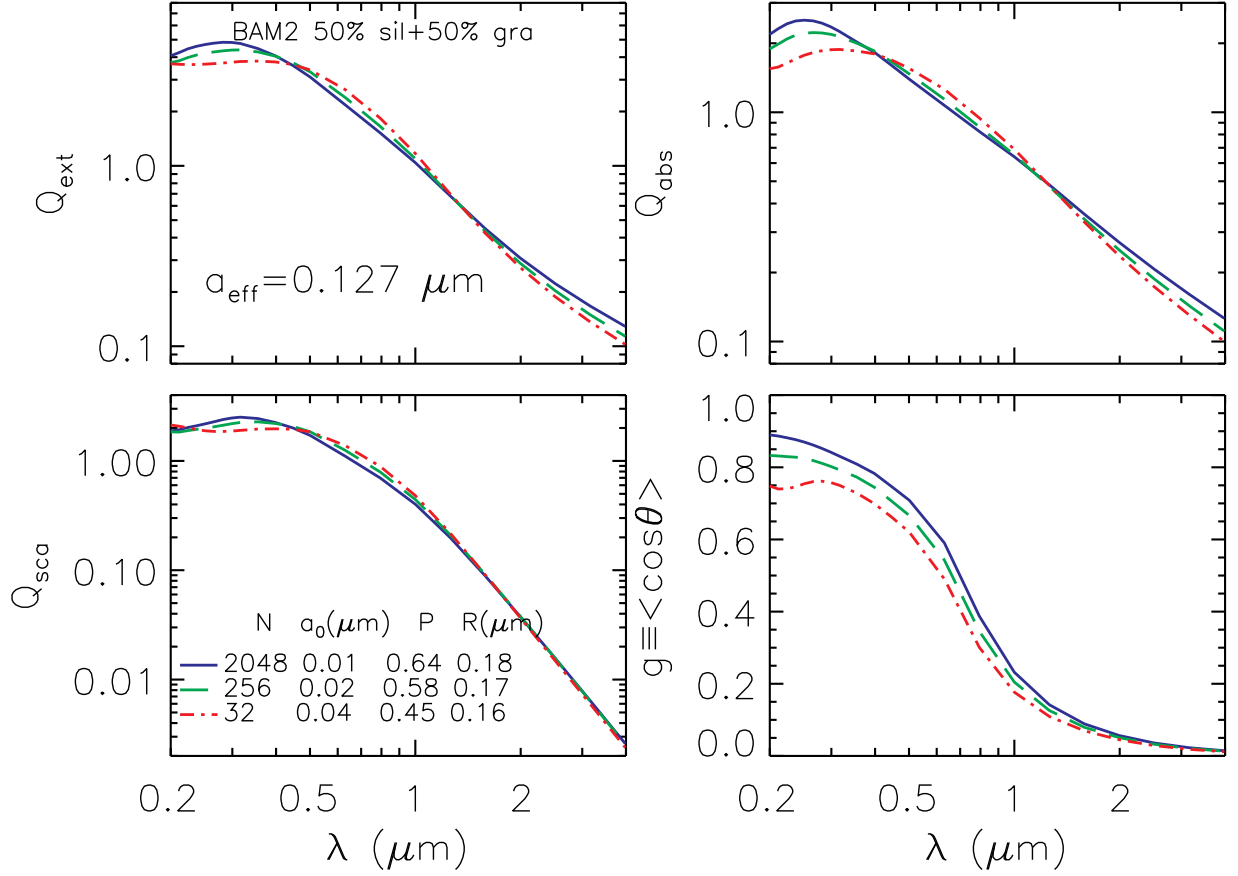


Fig. 7.— Q_{ext} , Q_{abs} , Q_{sca} and $g \equiv \langle \cos \theta \rangle$, for three BAM2 aggregates with 50% silicate and 50% graphite. These aggregates have the same amount of solid materials ($a_{\text{eff}} = 0.127 \mu\text{m}$) but different porosities ($P \approx 0.45, 0.58, 0.64$) for $N = 32, 256, 2048$. At a given λ , the computed Q_{abs} , Q_{ext} , and Q_{sca} are porosity-dependent, except at the “transition radii” $\lambda_t \approx 0.35 \mu\text{m}$ and $\sim 1.4 \mu\text{m}$ where the cross sections are insensitive to porosity. For $0.35 \lesssim \lambda \lesssim 1.4 \mu\text{m}$, the cross sections *decrease* as the porosity is increased.

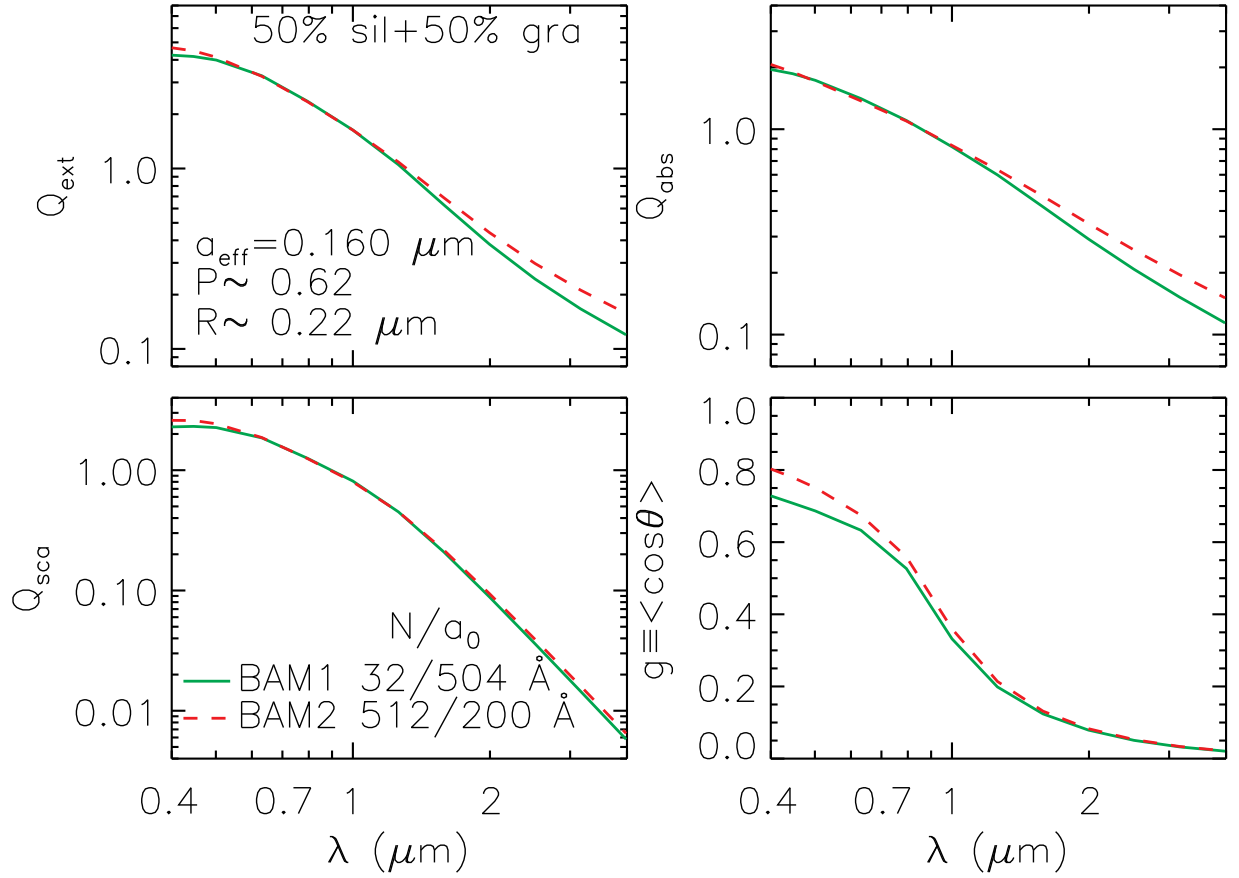


Fig. 8.— Comparison of two clusters with different geometries (BAM1 vs. BAM2), different monomer size but similar porosity $\mathcal{P} \approx 0.62$ and same $a_{\text{eff}} = 0.160 \mu\text{m}$. The optical properties are very similar. Therefore monomer size has no significant effects as long as monomers are smaller than the incident wavelength.

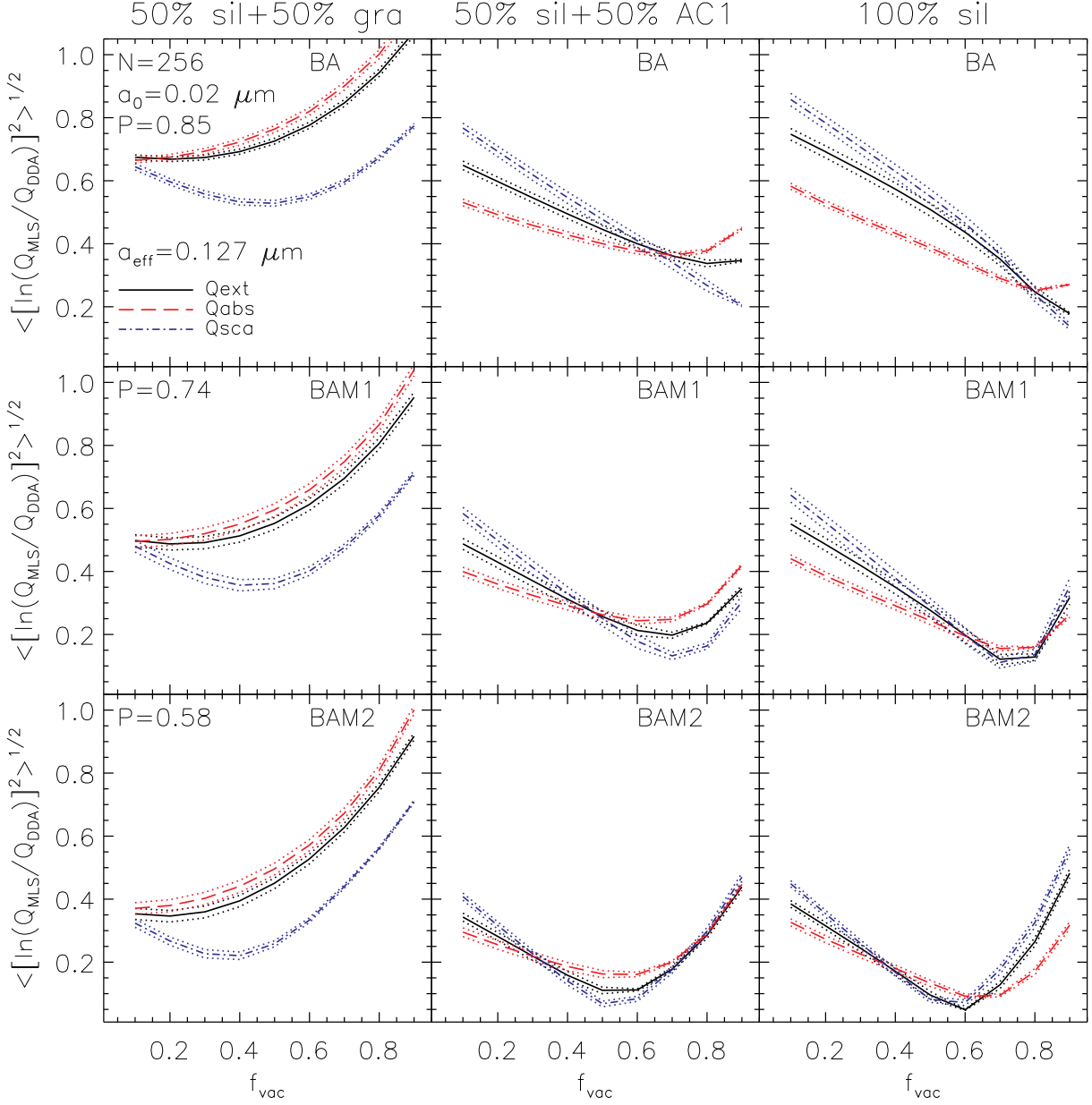


Fig. 9.— Global errors (defined in eqn. 19) for the MLS results and the DDA results for the fiducial aggregates as shown in Fig. 6. Dotted lines show the standard deviation from the 5 realizations.

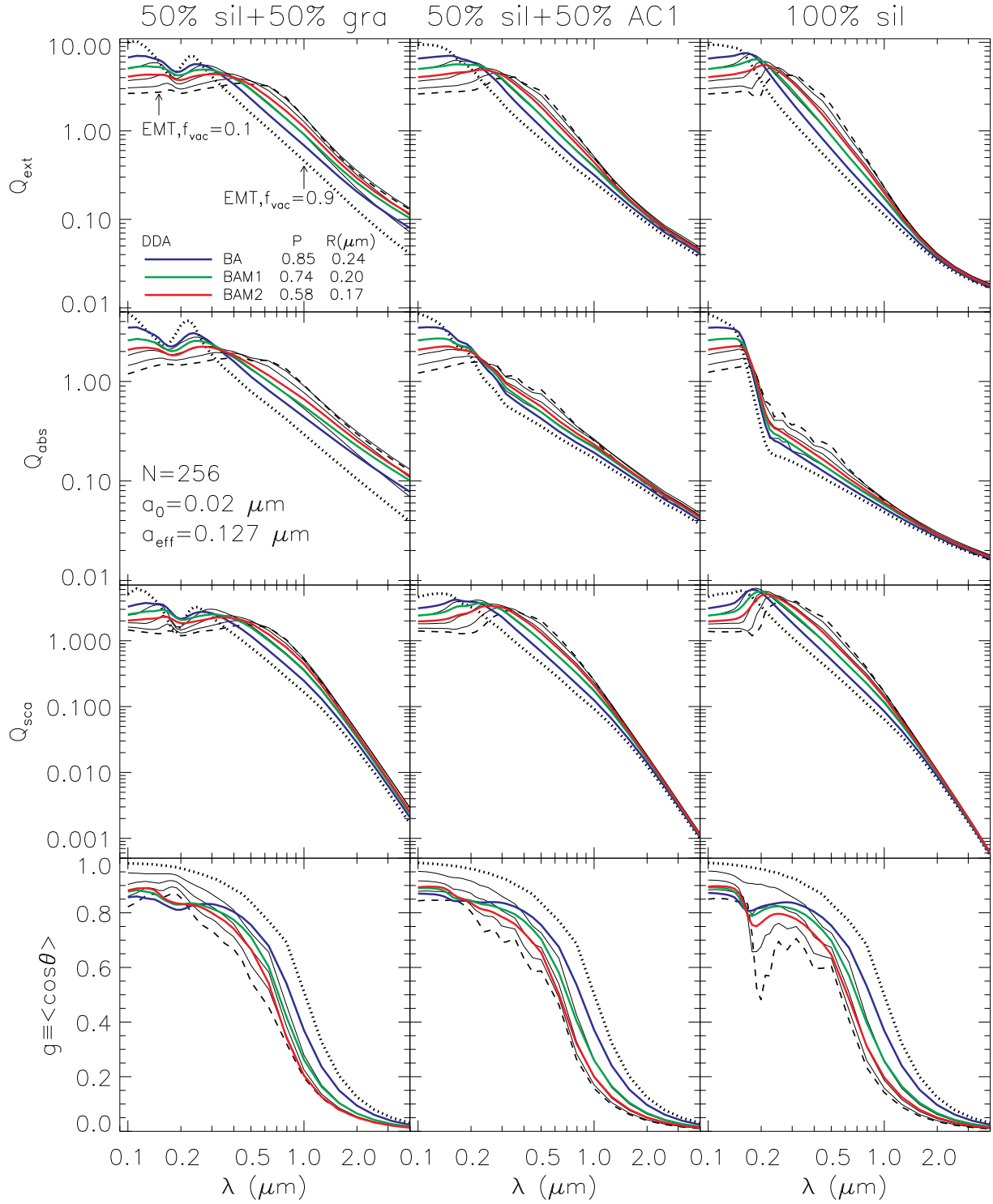


Fig. 10.— The same as Fig. 6, only with the MLS results replaced by the EMT-Mie results, for f_{vac} from 0.1 to 0.9.

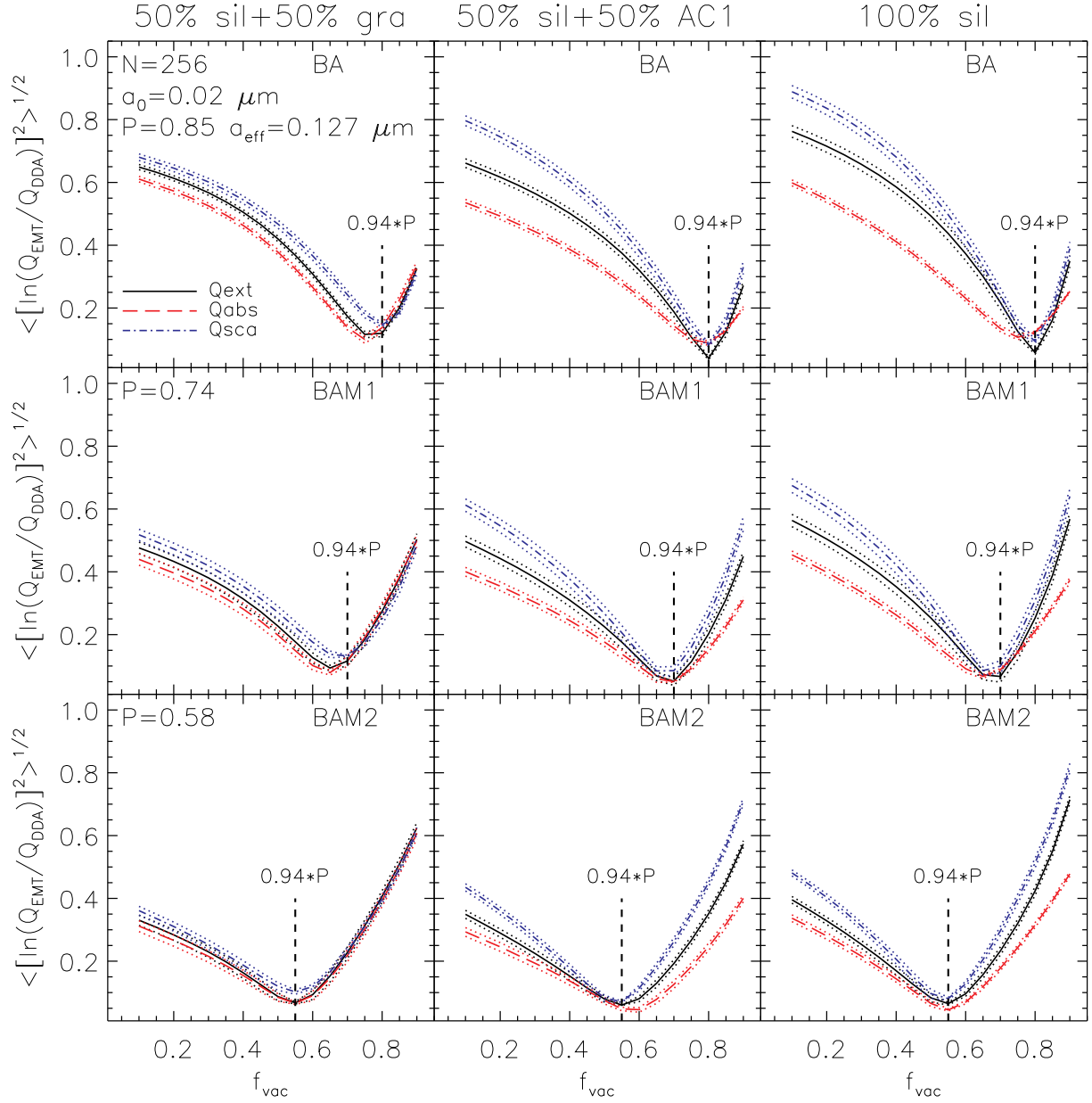


Fig. 11.— Global errors (similar definition as in eqn. 19) for the EMT-Mie results and the DDA results for the fiducial aggregates as shown in Fig. 10. f_{vac} from eq. (21) is shown.

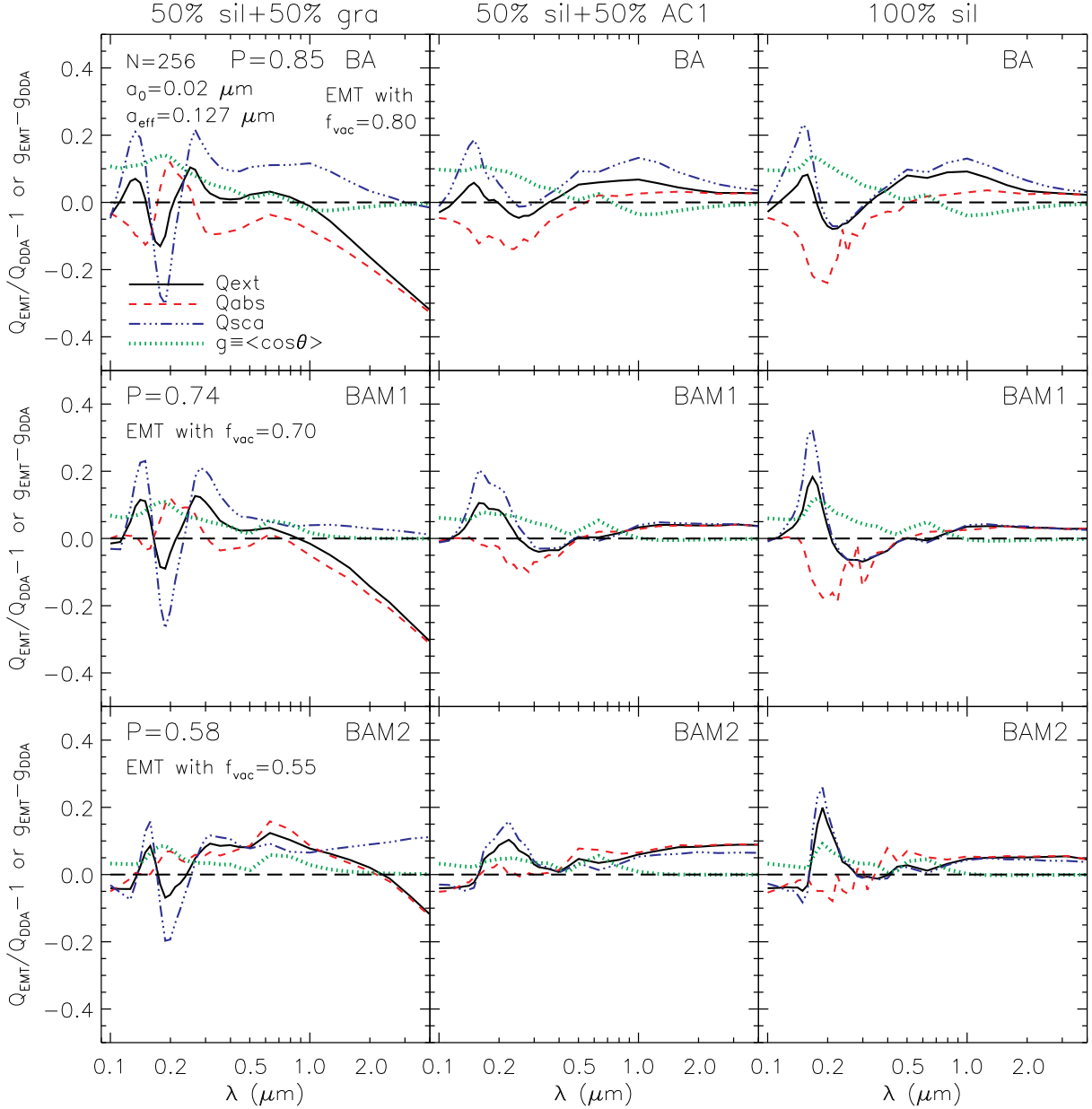


Fig. 12.— The difference between the optimal EMT-Mie results with $f_{\text{vac}} = 0.94P$ and the DDA results for our fiducial clusters. Plotted here are $(Q_{\text{EMT}}/Q_{\text{DDA}} - 1)$ for cross sections, and $(g_{\text{EMT}} - g_{\text{DDA}})$ for $g \equiv \langle \cos \theta \rangle$. The fractional difference is typically $\lesssim 20\%$ for total cross sections.